Distribution of trace elements in pyrite from carbonate-hosted sulfide deposits of southern British Columbia

S. Paradis[1*], S.E. Jackson[2], D. Petts[2], G.J. Simandl[3,4], R.J. D'Souza[3], and T.S. Hamilton[1]

Paradis, S., Jackson, S.E., Petts, D., Simandl, G.J., D'Souza, R.J., and Hamilton, T.S., 2022. Distribution of trace elements in pyrite from carbonate-hosted sulfide deposits of southern British Columbia; in *Targeted Geoscience Initiative 5: volcanic- and sediment-hosted massive-sulfide deposit genesis and exploration methods, (ed.) J.M. Peter and M.G. Gadd; Geological Survey of Canada, Bulletin 617, p. 129–163. https://doi.org/10.4095/328002*

Abstract: This paper combines petrography with in situ laser-ablation inductively coupled plasma mass spectrometry to document trace-element variations in pyrite (Py) from Mississippi Valley–type (MVT) and fracture-controlled replacement (FCR) deposits in the Kootenay Arc, British Columbia.

Three generations of pyrite are Py 1, Py 2, and Py 3. Pyrite 1, the earliest (occurring in MVT deposits only), has higher Ag, Ba, Cu, Ge, Pb, Sb, Sr, Tl, and V than adjacent Py 3. It has higher Ag, Au, Ba, Cu, Ge, Pb, and Tl than Py 2. Pyrite 2 occurs in MVT and FCR deposits. Relative to FCR Py 2, MVT Py 2 is enriched in Co, Ni, Mo, Ba, Tl, and Pb and depleted in other elements. The FCR Py 2 has growth-related compositional banding, which is absent in MVT Py 2. The FCR Py 2 has Ag, Cu, Ga, Ge, In, Sn, and Zn enriched cores, intermediate Au- and As-rich bands, and Co- and Ni-rich rims. Pyrite 3, the latest occurring pyrite, present in MVT and FCR deposits, is enriched in Co and Ni near overgrowths or infillings of sphalerite.

Variations in composition of Py reflect mineralogy, characteristics of ore-forming fluids, and differences in physicochemical conditions between MVT and FCR deposits at the time of ore deposition.

Résumé : Dans le présent article, nous combinons la pétrographie à la spectrométrie de masse avec plasma à couplage inductif jumelée à l'ablation par laser (LA-ICP-MS), in situ, pour documenter les variations des éléments traces dans la pyrite (Py) provenant de gîtes de type Mississippi-Valley (M-V) et de gîtes de remplacement contrôlé par des fractures (RCF) dans l'arc de Kootenay, en Colombie-Britannique.

Trois générations de pyrite (Py 1, Py 2 et Py 3) sont distinguées. La pyrite 1, la plus ancienne (présente dans les gîtes de type M-V seulement), renferme des concentrations de Ag, Ba, Cu, Ge, Pb, Sb, Sr, Tl et V supérieures à celles de la Py 3 adjacente. Elle renferme également de plus fortes teneurs en Ag, Au, Ba, Cu, Ge, Pb et Tl que la Py 2. Cette dernière est présente dans les gîtes de type M-V et les gîtes de RCF. Comparativement à la Py 2 des gîtes de RCF, la Py 2 des gîtes de type M-V est enrichie en Co, Ni, Mo, Ba, Tl et Pb, et appauvrie en d'autres éléments. La Py 2 des gîtes de RCF montre un rubanement de composition lié à la croissance cristalline, une caractéristique absente de la Py 2 des gîtes de type M-V, ainsi que des noyaux enrichis en Ag, Cu, Ga, Ge, In, Sn et Zn, des bandes intermédiaires riches en Au et en As, et des bordures riches en Co et en Ni. La pyrite la plus récente, la Py 3, est présente dans les gîtes de type M-V et les gîtes de RCF, et est enrichie en Co et en Ni à proximité d'accroissements secondaires ou de remplissages de sphalérite.

Les variations de composition de la pyrite sont un reflet de la minéralogie, des caractéristiques des fluides minéralisateurs ainsi que des différences dans les conditions physicochimiques entre les gîtes de type M-V et les gîtes de RCF au moment du dépôt de la minéralisation.

[1]Geological Survey of Canada, 9860 West Saanich Road, Sidney, British Columbia V8L 4B2
[2]Geological Survey of Canada, 601 Booth Street, Ottawa, Ontario, K1A 0E9
[3]British Columbia Geological Survey, British Columbia Ministry of Energy, Mines and Petroleum Resources, P.O. Box 9333, Stn Prov Gov't, Victoria, British Columbia V8W 9N3
[4]School of Earth and Ocean Sciences, University of Victoria, P.O. Box 1700 Stn CSC, Victoria, British Columbia V8W 2Y2
*Corresponding author: S. Paradis (email: suzanne.paradis@nrcan-rncan.gc.ca)

INTRODUCTION

The trace-element composition of pyrite from carbonate-hosted sulfide deposits is not well documented, whereas pyrite composition from sedimentary exhalative (SEDEX) and volcanogenic massive-sulfide (VMS) deposits are better studied. The focus of this contribution is to document compositional variations between pyrite from two types of carbonate-hosted sulfide deposits that occur in the Kootenay Arc of southern British Columbia: Mississippi Valley–type (MVT) and fracture-controlled replacement (FCR) deposits. These deposits form 1) stratabound ellipsoidal accumulations of sulfide minerals interpreted as Mississippi Valley–type (MVT) Zn-Pb deposits (e.g. Reeves MacDonald), and 2) fracture-controlled replacement (FCR) Zn-Pb-Ag-Au deposits (e.g. Abbott-Wagner). The deposits are distributed along the entire length of the Kootenay Arc, from Revelstoke in the north to beyond the Canada-U.S.A. border in the south (Fig. 1). Deposits are concentrated along the eastern edge of the Kootenay terrane and the FCR type is restricted to this tectonic boundary. Two main districts in the Kootenay Arc are defined in this paper as the Salmo district and the Duncan camp. The MVT Reeves MacDonald, Jersey-Emerald, and Jackpot deposits are located in the Salmo district, and the MVT Duncan deposit is located in the Duncan camp. The FCR Abbott-Wagner deposit is located north of the Duncan camp. The deposits are hosted by deformed lower Cambrian shallow-water platformal carbonate rocks of the Badshot Formation, and its equivalent, the Reeves member of the Laib Formation.

Pyrite is ubiquitous throughout the sulfide deposits in the Kootenay Arc and can incorporate numerous minor and trace elements (e.g. As, Ag, Au, Bi, Co, Cu, Hg, Mo, Ni, Pb, Sb, Se, Te, Tl, and Zn) into its crystal structure, or as micro-inclusions of other mineral phases (e.g. Gregory et al., 2015; Gadd et al., 2016; Dehnavi et al., 2018). The geochemical signature of pyrite can provide insight into the environment and conditions of its formation (Large et al., 2007, 2009, 2011; Gregory et al., 2015; Gadd et al., 2016). Numerous studies during the past decade have focused on the trace-element content of pyrite in fine-grained clastic sedimentary rocks (e.g. Large et al., 2009; Gregory et al., 2015; Gadd et al., 2016; Sack et al., 2018); however, to our knowledge there are few published studies on the trace-element content of pyrite from carbonate-hosted sulfide deposits.

In this paper, we present laser-ablation inductively coupled plasma mass spectrometry (LA-ICP-MS) analyses of pyrite from the Reeves MacDonald, Jersey-Emerald, Jackpot, and Duncan MVT deposits and from the Abbott-Wagner FCR deposit. Similar studies of pyrite and sphalerite from other deposits in the Kootenay Arc are ongoing and aim to provide further insight on migration and precipitation of metallic elements during mineralization events. Simandl et al. (this volume) present LA-ICP-MS analyses of dolomites associated with MVT deposits of the Kootenay Arc and Rocky Mountains and document their compositional differences.

GEOLOGICAL SETTING

The Kootenay Arc is part of the Kootenay terrane and lies within the Omineca Belt, one of five physiographic and tectonic belts of the Canadian Cordillera (Wheeler and McFeely, 1991; Monger and Price, 2002). The Omineca Belt consists of polydeformed and metamorphosed sedimentary, volcanic, and granitic rocks that are exposed east of Mesozoic arc and back-arc sequences of the Intermontane Belt and west of deformed Paleozoic continental margin sedimentary rocks (i.e. the Foreland Belt). The Kootenay terrane is predominantly composed of lower to mid-Paleozoic sedimentary and volcanic rocks that were deposited on the distal western margin of Ancestral North America (Gabrielse et al., 1991; Colpron and Price, 1995; Paradis et al., 2006).

The Kootenay Arc consists of a thick succession of thrust-imbricated Proterozoic to early Mesozoic miogeocline-platform to deep-marine strata of sedimentary and volcanic origin (Brown et al., 1981). This arcuate feature within the Kootenay Arc is a belt of complexly deformed rocks extending approximately 400 km long and starts north of Revelstoke, and runs to 14 km south of the Canada-U.S.A. border (Fyles, 1964). The Kootenay Arc, which lies between the Purcell anticlinorium in the Purcell Mountains to the east and the Monashee Complex to the west (Fig. 1), is of economic interest because it contains numerous carbonate-hosted Zn-Pb (±Ag, ±Au) deposits, among others.

Three phases of folding have been recognized within the Kootenay Arc (Fyles, 1964; Warren and Price, 1993). Initial, large-amplitude (10 km scale), west-verging, recumbent folds were deformed by two phases of upright, tight to isoclinal folds and these are associated with lower greenschist to amphibolite facies regional metamorphism. The low-grade regional metamorphism is locally overprinted by upper amphibolite facies contact metamorphism around Middle Jurassic and middle Cretaceous intrusions, and a narrow belt of Barrovian amphibolite facies rocks transects the central part of the Kootenay Arc (Moynihan and Pattison, 2013). The polyphase deformation in the Kootenay Arc resulted in pervasive transposition of bedding that locally obscures stratigraphic relationships (Colpron and Price, 1995). Colpron and Price (1995) outlined a regionally consistent stratigraphic succession along the Kootenay Arc, which is summarized below.

The lower part of the stratigraphic section along the Kootenay Arc is composed of Neoproterozoic–lower Cambrian siliciclastic rocks and carbonate rocks of the Hamill Group and Mohican Formation. These rocks are overlain by the lower Cambrian Archaeocyathid-bearing carbonate rocks of the Badshot Formation and its equivalent, the Reeves member of the Laib Formation (Fyles and Hewlett, 1959; Fyles, 1964), which host the Zn-Pb (±Ag, ±Au) sulfide deposits. The carbonate rocks are conformably

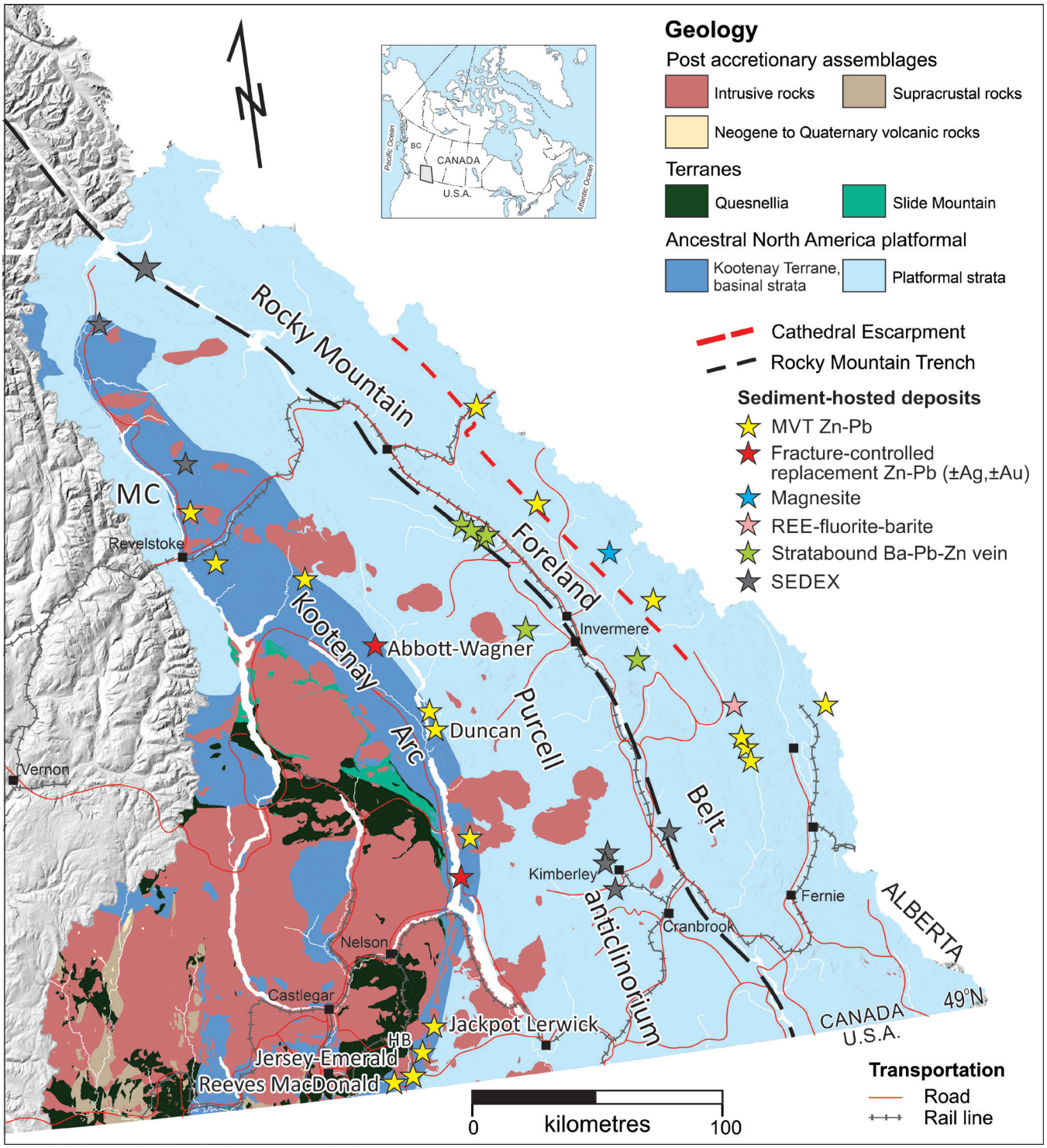

Figure 1. Regional geological map of southeastern British Columbia showing locations of carbonate-hosted sulfide deposits in the Kootenay Arc (dark blue). Deposits (stars) identified by name are discussed in this paper. The HB deposit is mentioned in the paper but not analyzed. The Kootenay terrane consists of the parautochthonous basinal strata (dark blue) of Ancestral North America, includes the Kootenay Arc, and extends west of the Monashee Complex (MC). This is a thrust bounded tectonostratigraphic package of Paleozoic rocks, which are folded, metamorphosed, intruded by plutons and mineralized. *Modified from* Katay (2017). Terranes *after* Cui et al. (2015).

overlain by lower Paleozoic siliciclastic, basinal shales and mafic volcanic rocks of the Lardeau Group (Colpron and Price, 1995).

ZINC-LEAD SULFIDE DEPOSITS

In the following descriptions and figures pertaining to the deposits and their samples, pyrites occurring in one or more of three distinct generations and morphological types (pyrite 1, pyrite 2, and pyrite 3) are referred as 'Py 1', 'Py 2', and 'Py 3', respectively; their morphologies and parageneses are summarized at the end of this section.

Reeves MacDonald MVT deposit

The Reeves MacDonald MVT deposit contains several orebodies (e.g. Reeves, MacDonald, O'Donnell, Annex, Point, Prospect, B.L., No. 4, and Red Bird) that together comprise the Reeves MacDonald mine. These orebodies are all believed to be fault-displaced segments of a single primary ore zone located along the axis of the Reeves syncline. Their combined production from 1949 to 1971 totaled 5 817 828 t of sulfide ore grading 3.48 weight per cent Zn and 1.39 weight per cent Pb (BC MINFILE 082FSW026; British Columbia Geological Survey, 2013). The orebodies occur discontinuously along an east-west trend over a distance of approximately 4 km. The sulfide zones, exclusively mined at Reeves, Annex, B.L., and O'Donnell, are enclosed by dolomitic limestone within the lower Cambrian Reeves member limestone (Laib Formation), typical of most carbonate-hosted Zn-Pb deposits in the southern Kootenay Arc. The area is characterized by east-striking foliation and southwest-trending fold axes. A series of north-striking faults dipping 25 to 45°E offset the host rocks and the mineralized zones (*see* the maps of Fyles and Hewlett, 1959). The mineralized zones form lenses and layers of massive to disseminated sulfides, parallel to compositional layering within medium to dark grey dolomitic limestone. The predominant sulfides are pyrite and sphalerite, with minor galena and traces of chalcopyrite.

The sample selected for this study (08-SP-77B) consists of semi-massive to massive polycrystalline clusters of pyrite with traces of galena and sphalerite in a matrix of dolomite and calcite, with cavities filled by secondary sparry calcite. In this sample, pyrite aggregate is a fine-grained mass with some domains (or regions) that are rich in mineral inclusions and others that are poor in mineral inclusions (Fig. 2a, b). This is accompanied by textural evidence of pressure solution and cataclastic flow associated with the dominant Mesozoic to Cenozoic deformation. The preserved inclusion-rich pyrite (Py 2) generally forms elongated and heterogeneous aggregates with fractures and inclusions of other sulfide phases and carbonates. Locally, pyrite crystals may be bent. The inclusion-poor domains are subhedral to euhedral, fractured pyrites (Py 3) that tend to occur on the periphery of the inclusion-rich pyrite domains (Fig. 2b). Pyrite 3 is more massive and commonly has a granoblastic polygonal texture with 120° grain boundaries, likely formed during tectonic deformation and metamorphism that post-dated mineralization. More ductile minerals like sphalerite and galena locally fill fractures and are enclosed as subspherical blebs within pyrite.

Jersey-Emerald MVT deposit

The Jersey-Emerald deposit encompasses the former Jersey and Emerald Zn-Pb mines. The Jersey and Emerald deposits together have produced more than 8 000 000 t, grading 3.83 weight per cent Zn and 1.95 weight per cent Pb (Giroux and Grunenberg, 2014). The deposits are located on the east limb of a regional north-northeast-trending anticline known locally as the Jersey anticline, and mineralization appears to be controlled by phase II (F2) secondary folds with thicker sulfide zones in the synclines rather than in the crest and limbs of the anticlines (Fyles and Hewlett, 1959; Bradley, 1970). Mid-Cretaceous granitic intrusions are elongated parallel to the regional foliation; they intersect the Jersey anticline and locally crosscut the Zn-Pb mineralization, where they have produced late-stage tungsten skarn mineralization.

Figure 2. Photomicrographs (reflected light) of studied samples from Mississippi Valley–type and fracture-controlled replacement deposits in the Kootenay Arc: **a)** aggregate of fine-grained inclusion-rich pyrite (Py 2) and inclusion-poor pyrite (Py 3) in sample 08-SP-77B from the Reeves MacDonald deposit; **b)** inclusion-rich pyrite core (Py 2) surrounded by inclusion-poor recrystallized pyrite (Py 3) in sample 08-SP-77B from the Reeves MacDonald deposit; **c)** pyrrhotite (Po) and galena (Gn) in sphalerite (Sph) matrix in sample JS-07-56.9 from the Jersey-Emerald deposit. The Sph, Po, and Gn are oriented parallel to foliation; **d)** irregularly shaped, anhedral grains of pyrite (Py 3 ≤1 mm) admixed with Sph, Po, and Gn in sample JS-07-56.9 from the Jersey-Emerald deposit; **e)** fractured and brecciated, anhedral pyrite (Py 3) in a matrix of deformed Sph and Po in sample 08-SP-102B from the Jackpot Lerwick zone; **f)** anhedral, fractured pyrite (Py 3) in Po and marcasite (Mrc); in sample 08-SP-102B from the Jackpot Lerwick zone; **g)** subrounded anhedral pyrite with inclusion-rich core (Py 1) and a rim of inclusion-free euhedral pyrite (Py 3) in sample 08-SP-121 from the Duncan no. 1 zone; **h)** inclusion-rich, subrounded pyrite grains (Py 1) in sample 08-SP-121 from the Duncan no. 1 zone; **i)** subhedral fractured pyrite (Py 2) with micro-inclusions of chalcopyrite (Cp), Sph, and carbonate (Carb) in sample 08-SP-155 from the Abbott-Wagner deposit; **j)** aggregate of polygonal pyrite grains (Py 3) showing annealed crystals with 120º triple junctions in sample 08-SP-155 from the Abbott-Wagner deposit.

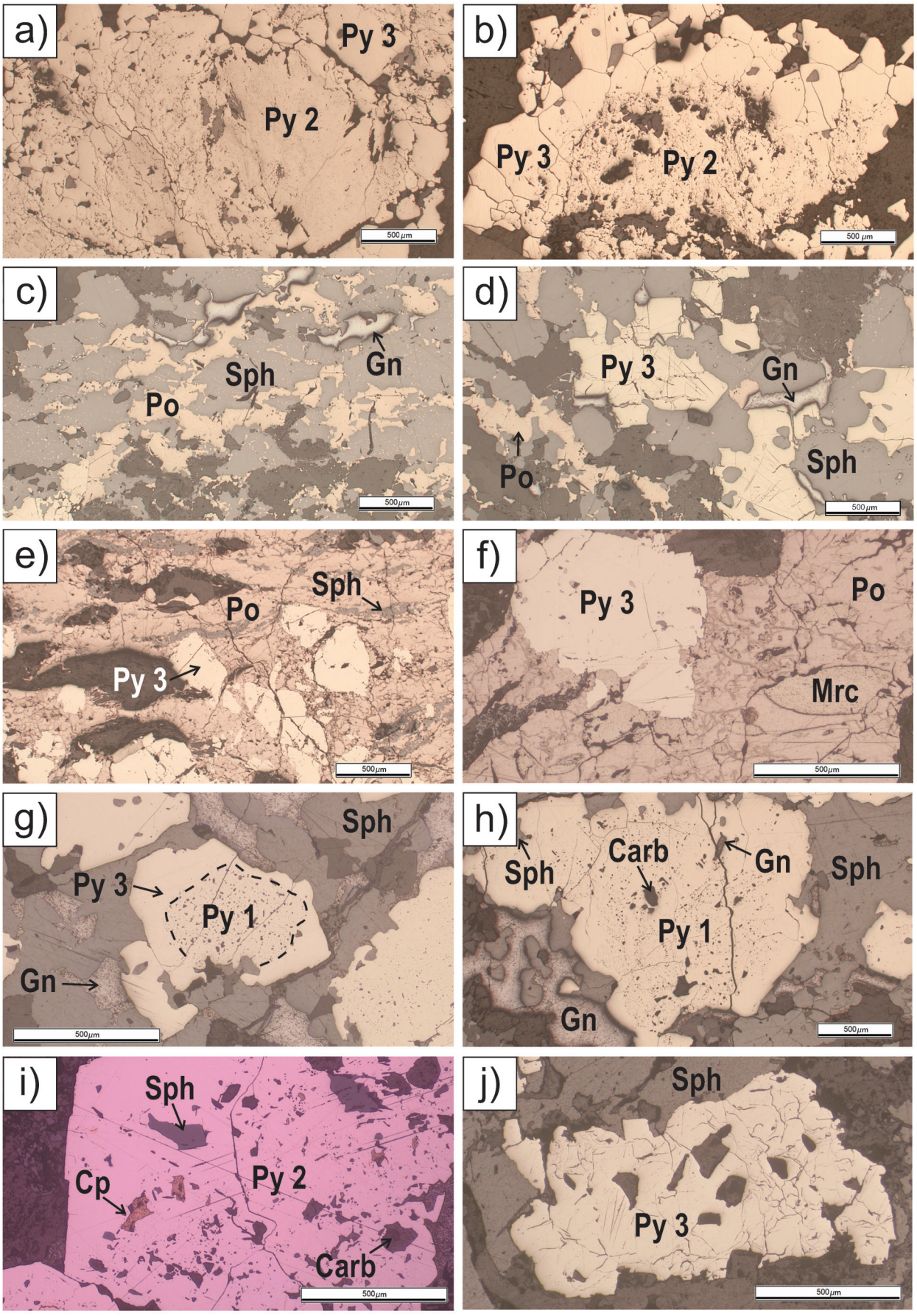
a)
Py 3
Py 2
500 µm
b)
Py 3
Py 2
500 µm
c)
Sph
Gn
Po
500 µm
d)
Py 3
Gn
Po
Sph
500 µm
e)
Sph
Po
Py 3
500 µm
f)
Py 3
Po
Mrc
500 µm
g)
Sph
Py 3
Py 1
Gn
500 µm
h)
Sph
Carb
Gn
Sph
Py 1
Gn
500 µm
i)
Sph
Cp
Py 2
Carb
500 µm
j)
Sph
Py 3
500 µm

The Zn-Pb sulfide mineralization is mainly confined to a dolomitized zone near the base of the lower Cambrian Reeves member limestone (Fyles and Hewlett, 1959; Bradley, 1970). There are five Zn-Pb dolomite-hosted sulfide layers ('bands') within the mine, each ranging in thickness from 0.3 to 9 m. These bands, from lowest to highest stratigraphic position, are: lower Pb band, lower Zn band, middle Zn band, upper Zn band, and upper Pb band. Another Zn-Pb-bearing dolomite horizon, 55 to 60 m below the former Jersey-Emerald Zn-Pb deposit, was intersected by drilling in 1995 (Paradis et al., 2015; Apex Mineral Resources Inc., no date). The sulfide mineralization forms stratabound, tabular and lens-shaped accumulations of pyrite, sphalerite, galena, pyrrhotite, and minor arsenopyrite in dolomite- and calcite-rich zones. Brecciated domains are common within the massive-sulfide mineralization. The mineralogy of the ore minerals is similar to the Reeves MacDonald and HB MVT deposits.

The sample (JS-07-56.9) selected for this study is a grey, finely layered dolostone-limestone with layers of fine- to medium-grained sulfide minerals parallel to the foliation (Fig. 2c). Large Py 3 grains (≤1 mm) admixed with sphalerite, pyrrhotite, and galena are less deformed, and display embayments and fractures filled by other sulfide minerals (Fig. 2d). Typically, pyrite, pyrrhotite, and galena occur as irregularly shaped anhedral grains in sphalerite matrix. The pyrite analyzed (Py 3) is a small (<250 μm), anhedral grain in sphalerite oriented parallel to foliation.

Jackpot MVT deposit

The Jackpot orebodies are stratabound, MVT, replacement Zn-Pb sulfide deposits in dolomitized limestone of the lower Cambrian Reeves member (Laib Formation; Fyles and Hewlett, 1959). At least four mineralized zones (Jackpot Main, Jackpot Lerwick, Jackpot West, and Jackpot East) have been discovered, with a total of 943 250 t of indicated ore, grading 4.68% combined Pb+Zn, and an additional 2 930 000 t of inferred ore (BC MINFILE 082FSW012; British Columbia Geological Survey, 1991).

The main sulfide minerals are sphalerite, pyrrhotite, pyrite, marcasite, and traces of galena. They form concordant lenses and layers oriented parallel to foliation within a matrix of recrystallized and altered carbonate minerals (i.e. dolomite and calcite). All minerals show some degree of deformation, with pyrite being the least deformed sulfide mineral. Pyrite occurs as isolated, irregular, anhedral crystals (1 mm in diameter) or as aggregates of brecciated and fractured anhedral to subhedral crystals enveloped in massive pyrrhotite and its alteration mineral, marcasite (Fig. 2e, f). Sphalerite, which occurs as discontinuous strings oriented parallel to foliation, is also replaced and enveloped by pyrrhotite. The fractures in pyrite are filled with more ductile sulfide minerals such as sphalerite and pyrrhotite. The sample of Py 3 selected for this study (08-SP-102B) is from the Jackpot Lerwick zone and is an anhedral, fractured grain enveloped in pyrrhotite and sphalerite (e.g. Fig. 2f).

Duncan MVT deposit

Although MVT Zn-Pb sulfide mineralization in the Duncan Lake area has been extensively explored, none of the deposits (Duncan no. 1 to 8 zones) have been mined. The main Duncan no. 5 to 8 zones are reported to have reserves of 9 000 000 t grading 2.9% Zn and 2.7% Pb (Muraro, 1962). The deposits consist of deformed and faulted sulfide bodies replacing thick sections of dolomitized and silicified carbonate rocks of the Badshot Formation on the hinge of a phase II (F2) fold on the east limb of the Duncan anticline, which is a major, phase I (F1), isoclinal fold (Höy, 1982). The deposits are interpreted to be MVT and the carbonate rocks hosting them are light to dark grey, massive or layered marble, or dolomitic marble, with mottled and flecked textures identical to the dolomite enclosing the sulfide deposits of the Salmo district. Höy (1982) interpreted the Badshot carbonate rocks in this area as an "extensively brecciated and locally dolomitized bank margin facies developed on a shoal complex".

The sulfide bodies are subvertical lenses and sheets of sulfide minerals with gradational but generally well-defined margins. The sulfide bodies are essentially parallel to the enclosing formations, with steep dips and low plunges to the north (i.e. the largest dimension is parallel to the strike and the intermediate dimension is parallel to the dip; Fyles, 1964). The orebodies plunge northward, parallel to the most prominent lineation and axes of F2 folds in the surrounding rocks.

Local mineralization consists of fine-grained pyrite, with subordinate sphalerite, galena, and pyrrhotite forming layers, lenses, and disseminations in the dolomite and siliceous dolomite of the Badshot Formation. Minor chalcopyrite, marcasite, pyrargyrite (Ag_3SbS_3), and meneghinite ($Pb_{13}CuSb_7S_{24}$) are also reported by Muraro (1962).

The sample (08-SP-121) selected for this study is from the Duncan no. 1 zone. It consists of fine- to coarse-grained, polycrystalline clusters of pyrite, sphalerite, galena, and traces of pyrrhotite in a dolostone matrix. The pyrite grain analyzed (e.g. Fig. 2g) has a subrounded to subangular, anhedral core rich in sulfide and carbonate inclusions (Py 1), surrounded by a rim of inclusion-free, euhedral pyrite (Py 3). The pyrite grain is surrounded by sphalerite, galena, and dolomite, which also fill fractures in Py 3. The inclusions in Py 1 consist of carbonate minerals, sphalerite, galena, and possibly other sulfide minerals (Fig. 2h; some grains are too small for optical identification). The inclusion-rich Py 1 is the earliest pyrite, and the inclusion-free, euhedral Py 3 overgrowth is the latest.

Abbott-Wagner FCR deposit

The Abbott-Wagner deposit is a polymetallic, FCR Zn-Pb-Ag-Au sulfide deposit hosted in the upper part of the Badshot Formation and the basal part of the overlying Index Formation. Mineralization occurs as sulfide-rich quartz veins in calcareous and carbonaceous phyllites and phyllitic schists of the Index Formation, and as lenses of massive to semi-massive sulfide minerals replacing carbonate rocks of the Badshot Formation. The total historical mineral resource in two zones at Abbott is estimated to be 39 030 t grading 10.26 weight per cent Pb, 16.12 weight per cent Zn, 286.3 g/t Ag, and 1.2 g/t Au (noncompliant with National Instrument 43-101; BC MINFILE 082KNW056; British Columbia Geological Survey, 2011). Replacement mineralization in carbonate rocks consists of clustered and disseminated galena, sphalerite, and pyrite, with traces of chalcopyrite and tetrahedrite in quartz-calcite gangue replacing the dolomite matrix and cementing brecciated fragments of carbonate rocks and phyllites.

The sample (08-SP-155) selected for this study is a polycrystalline mass of sphalerite, pyrite, and galena with traces of chalcopyrite. Pyrite and galena in this sample are mostly enveloped by sphalerite. Chalcopyrite only occurs as very fine inclusions in pyrite. The Py 2 analyzed occurs as irregular anhedral to subhedral grains (≤1.5 mm in diameter) with embayments enveloped by sphalerite, locally accompanied by galena. This Py 2 (Fig. 2i) has moderately abundant inclusions of carbonate, sphalerite, and chalcopyrite; the larger grains tend to have fractures filled by galena and sphalerite. This Py 2 is always associated with sphalerite and is interpreted to have a hydrothermal origin (*see* below). Another less common type of pyrite (Py 3) forms overgrowths on Py 2 or occurs as small (<0.1 mm in diameter) euhedral, cubic to cuboctahedral crystals, disseminated or forming aggregates of annealed crystals with 120º grain boundaries in carbonate minerals and sphalerite (Fig. 2j). Such textures in pyrite typically indicate recrystallization and grain growth during metamorphism or rheomorphism.

Summary of pyrite morphologies and textures

All three morphological types of pyrite (Py 1, Py 2, and Py 3), corresponding to different parageneses, occur in the MVT deposits studied. Only Py 2 and Py 3 occur in the Abbott-Wagner FCR deposit (Table 1).

1. Pyrite 1 occurs as subrounded, inclusion-rich cores (<500 µm in diameter; Fig. 2g). It has only been identified in MVT deposits, specifically the Duncan no. 1 deposit, where it is surrounded by a later pyrite generation (Py 3; Fig. 2g). Pyrite 1 commonly occurs as cores to Py 2 and Py 3 and is the earliest pyrite observed. As such, Py 1 is interpreted to have a sedimentary origin, possibly forming early during diagenesis. A sedimentary origin is supported by its timing relative to Py 2 and Py 3 and by its geochemical characteristics (*see* Results); however, we cannot rule out early formation from hydrothermal fluid.
2. Pyrite 2 occurs as anhedral to subhedral grains that are moderately rich in inclusions (Fig. 2a, b, and i). Individual crystals or crystal aggregates are commonly fractured and enclosed in sphalerite or pyrrhotite. Pyrite 2 contains fractures filled by more ductile sulfide minerals (e.g. sphalerite, pyrrhotite, and galena). It occurs in MVT and FCR deposits and can be overgrown by later pyrite (Py 3). Pyrite 2 is always associated with other sulfide minerals, and is interpreted to have formed during hydrothermal fluid flow.
3. Pyrite 3 is the latest pyrite. It typically has sharp and well-defined crystal boundaries, displays euhedral shapes (cubes, octahedra, and pyritohedra), and is free of inclusions. It is disseminated within the carbonate matrix, and can form porphyroblasts, aggregates of annealed pyrite grains with 120° grain boundaries, or overgrowths on earlier pyrite cores (Fig. 2b, d, e, f, g, j). Locally, individual grains and aggregates of Py 3 are oriented parallel to foliation. Pyrite 3 occurs in MVT and FCR deposits and is interpreted to result from recrystallization of pre-existing pyrite and possibly from Fe and S migration with fluids during metamorphism or rheomorphism.

METHODS

A suite of polished thin sections and 100 µm thick blocks were made from representative samples of sulfide deposits in the Kootenay Arc of southern British Columbia. We used petrographic microscope analysis to complete detailed examinations of each sample to identify the minerals, textures, and paragenesis and select areas suitable for LA-ICP-MS analysis.

We used LA-ICP-MS to measure the content of S, V, Fe, Co, Ni, Cu, Zn, Ga, Ge, As, Se, Mo, Ag, Cd, In, Sn, Sb, Ba, Au, Tl, Pb, and Bi in pyrite from MVT Zn-Pb sulfide (Reeves MacDonald, Jersey-Emerald, Jackpot Lerwick, Duncan) and FCR Zn-Pb-Ag-Au sulfide (Abbott-Wagner) deposits of the Kootenay Arc. Other elements were also measured during the analytical sessions (e.g. major elements, high field strength elements, and rare-earth elements (REEs)). Elements that likely occur as silicate and carbonate inclusions in sulfides (Na, Mg, Al, Si, P, K, Ca, Ti, and Mn) are reported as oxides. The content of some elements (e.g. high field strength, REE, and others) are not reported in this paper for one or more of the following reasons: 1) some of the measured values were semi-quantitative (C, P, and Te); 2) the measured values were at or below the detection limits (e.g. B, Nb, Hf, and REE); or 3) the elements were not measurable in the USGS GSE-1G standard used (e.g. Hg).

The LA-ICP-MS analyses consisted of five 2-D element maps that were acquired at the Geological Survey of Canada (Ottawa, Ontario) using an Agilent 7700x

Table 1. Characteristics of different pyrite generations in Mississippi Valley–type and fracture-controlled replacement deposits.

	Pyrite 1 (Py 1)	Pyrite 2 (Py 2)	Pyrite 3 (Py 3)
Mississippi Valley–type Zn-Pb			
Texture	Subrounded grains, inclusion-rich (carbonate minerals, galena), and surrounded by later pyrite generation (Py 3)	Fine-grained aggregate of inclusion-free and inclusion-rich domains; fractured; or surrounded by Py 3	Euhedral shape that forms octahedra and pyritohedra; typically inclusion-free; disseminated in matrix or overgrows previous pyrites
Diameter	<500 µm	<1000 µm	Variable; typically <500 µm
Trace element concentration (ppm)	0.01–100s (except Pb = 100 000s)	0.01–1000s (except Zn and Pb = 100 000s)	Duncan: 0.1–10s (except Zn and Pb >1000s); J-E: 0.1–1000s (except Zn, Pb >10 000s and Ni, Cd >1000s); J-L: 0.01–1000s (except Zn, Pb >10 000s and Cu, Ba, V >1000s)
Element enrichment	Na_2O, K_2O, CaO, MnO, and MgO, and V, Cu, Ge, Ba, Sr, Ag, Sb, Tl, and Pb compared to adjacent Py 3	Co, Ni, Mo, Ba, Tl, and Pb compared to FCR Py 2	Most elements (except Au, As) compared to FCR Py 3
Fracture-controlled replacement Zn-Pb-Ag-Au			
Texture	n/a	Subhedral, moderate inclusions of other sulfides; fractured; and within matrix of sphalerite	Euhedral, cubic to cuboctahedral crystals; aggregates of annealed crystals
Diameter	n/a	<5000 µm	Variable; typically <100–500 µm
Trace element concentration (ppm)	n/a	0.01–100 000s (except Cu, Zn, Pb >100 000s)	0.01–1000s (except Zn = 100 000s)
Element enrichment	n/a	Au, As compared to MVT Py 2	Au, As compared to MVT Py 3

Abbreviations: FCR: fracture-controlled replacement; J-E: Jersey-Emerald; J-L: Jackpot Lerwick; MVT: Mississippi Valley–type; n/a: not applicable; Py: pyrite

quadrupole ICP-MS coupled to a Teledyne Photon Machines Analyte G2 excimer laser ablation system (λ = 193 nm). Selected isotopes were measured using a fast time-resolved analysis acquisition protocol, providing signal intensity in counts per second (cps) for each mass measured.

Elemental mapping was carried out on the selected areas of each thick section using the instrumentation described, following the procedure of Lawley et al. (2015, 2017). Element maps were constructed by acquiring ICP-MS data while moving the sample under a focused laser beam to form a series of line scans covering the region of interest. The laser was operated at 4.0 to 4.4 J/cm^2 fluence, with a 30 Hz repetition rate, using a spot diameter ranging from 4 to 40 µm and a scan speed of 4 to 80 µm/s. The spot size and scan speed were selected so that the sample stage advances the equivalent spot diameter every 0.5 s (for beam diameters >10 µm), or every 1 s (for beam diameters <10 µm). For example, for a 20 µm diameter beam the sample was moved at 40 µm/s, whereas for a 6 µm diameter beam the sample was moved at 6 µm/s. For regions with very fine grained inclusions and fractures, this means that the recorded elemental spectrum represents a mixture of the minerals within the analyzed area. Each ablation pass was preceded by a cleaning step that involved rapidly ablating the sample surface at a rate of 2 to 3 pulses per spot diameter, followed by 50 to 60 s for washout. Every ablation pass also involved the collection of 20 s of background (i.e. gas blank) measurement prior to sample ablation. The ablation aerosol was transported out of the HelEx II sample cell through approximately 1 m of 2 mm (inner diameter) Teflon tubing (no SQUID smoothing device attached) using He at 1 L/min. The aerosol and He carrier gas were mixed with Ar (approximately 1 L/min) before entering the ICP-MS. The ICP-MS was tuned on NIST-612 glass to achieve greater than 9000 cps/ppm on ^{175}Lu (50 µm spot, approximately 7 J/cm^2 at 10 Hz), while minimizing the production of oxides (<0.2% for ThO^+-Th^+) and maintaining a U^+-Th^+ ratio of approximately 1.0. The total sweep time to measure all masses on the ICP-MS (in time-resolved analysis mode) was 250 ms. For maps produced using a spot diameter greater than 10 µm, these settings allowed for two full scans of the

mass spectrometer every 0.5 s (the equivalent of one spot diameter along the line scan). For maps produced using a smaller spot size, four full sweeps of the analyzed masses were achieved over sample stage travel of one spot diameter. Dwell times were optimized based on expected count rates of the minerals of interest and the natural abundance of the specific isotope used in the acquisition method (e.g. Fe, S, Zn, Na, Al, and Si were measured for 1 to 4 ms; V, Co, Ni, Cu, Mo were measured for 4 to 6 ms; and As, Ag, Au, and Bi were measured for 6 to 12 ms).

Standardization was achieved by calibrating the signals of unknowns against analyses of USGS GSE-1G (for most major and trace elements; Guillong et al., 2005) and in-house reference materials of pyrrhotite (sulfur calibration) and calcite (carbon calibration), then normalizing the total element or element oxide concentrations to 100% (Halicz and Günther, 2004) to correct for differential ablation yields of the various mineral phases. Calibration standards were analyzed every 20 unknowns (approximately once every hour) to account for instrument drift during the mapping runs. Secondary reference standard NIST-610 was analyzed every 20 unknowns and routinely yielded calculated concentrations within 10 to 15% of the accepted values for most elements. Reference values for GSE-1G and NIST-610 are 'GeoReM preferred values' taken from the GeoReM online geological and environmental reference materials database (Jochum et al., 2005). All data processing was performed using in-house software at GSC Ottawa: LAMTrace and PixeLAte. Maps were then constructed using the georeferenced elemental concentration outputs from PixeLAte with an in-house Python script at GSC Ottawa that generates false-colour, 2-D images using a percentile scaling function, with warm and cool colours representing high and low concentrations, respectively. The spatially indexed elemental concentration data were also imported to ioGAS™ and subsequently analyzed and interpreted using both spatial and chemical concentration discriminants.

RESULTS

On element maps (Fig. 3–7), the various pyrite generations can be identified by their textural features and differing compositions. All three of the pyrite generations (Py 1, Py 2, Py 3) assessed in this paper have been documented in MVT deposits, whereas only Py 2 and Py 3 have been identified in the Abbott-Wagner FCR deposit (Table 1).

Trace-element compositions of each pyrite generation are summarized below, and statistical information (extracted from the concentration map files using ioGAS) is presented in Tables 2 and 3. In general, the trace-element contents in analyzed MVT pyrite grains are lower than in analyzed FCR pyrite grains. Typically, trace-element contents in MVT deposits range from one tenth to thousands of parts per million (except for Pb and Zn, which can be more than 100 000 ppm); however, in the Abbott-Wagner FCR deposit, they range from one tenth to hundreds of thousands of parts per million (except for Cu, Pb, and Zn, which can each be more than 100 000 ppm). The high values of Cu, Pb, and Zn in pyrite from both MVT and FCR deposits are most likely the result of sampling galena, sphalerite, and chalcopyrite inclusions, overgrowths, fracture fills, and/or adjacent grains because the pyrite structure and stoichiometry cannot accommodate such high concentrations of these elements.

Pyrite can readily incorporate small amounts of numerous trace elements, including Ag, As, Au, Bi, Co, Cu, Hg, Mo, Ni, Pb, Sb, Se, Te, Tl, and Zn, into its crystal lattice. Elements such as Ag, As, Bi, Cd, Cu, Mn, Mo, Pb, Sb, Tl, and Zn may reside either in the pyrite crystal lattice or in sulfide mineral inclusions (Large et al., 2014; Gregory et al., 2015). At low concentrations, Ag, Au, Bi, Cu, and Pb occur uniformly in the pyrite structure; however, at high concentrations they tend to occur as micro-inclusions (Gregory et al., 2015). Zinc and cadmium also occur as micro-inclusions of sphalerite in pyrite. Other elements, such as Co and Ni, are easily incorporated in the pyrite crystal lattice, where they can substitute for Fe2+ and are not easily released during hydrothermal or metamorphic pyrite recrystallization (Morse and Luther, 1999; Tribovillard et al., 2006; Large et al., 2009; Gregory et al., 2015).

Pyrite 1

The subrounded, inclusion-rich Py 1 grains at the Duncan deposit (sample 08-SP-121; Fig. 2g and 3) have higher Na_2O, K_2O, CaO, MnO, MgO, Ag, Ba, Cu, Ge, Pb, Sb, Sr, Tl, and V contents than adjacent Py 3 grains (Fig. 8; Table 2), likely due to fine-grained inclusions or association of different mineral assemblages during their formation. Typically high Na, K, Ca, Mn, Mg, Ba, and Pb content corresponds to the presence of silicate, carbonate, and sulfide inclusions in pyrite. Pyrite 1 has less As, Co, and Ni than Py 3 (Fig. 8; Table 2). A linear transect intersecting Py 1 and Py 3 (Fig. 9) shows these contrasting compositional trends.

In MVT deposits, Py 1 has less As, Ba, Cd, Co, Ga, Mo, Ni, Se, Sb, V, and Zn and more Ag, Au, Ba, Cu, Ge, Pb, and Tl than Py 2 (Table 2). In pyrite from MVT deposits, Ge ranges from 3.2 to 50 ppm in Py 1 and from 0.16 to 19 ppm in Py 2. Similar ranges of Tl are present in MVT Py 1, Py 2, and Py 3 (Py 1 = 18–180 ppm; Py 2 = 0.01–100 ppm; Py 3 = 0.01–92 ppm). Copper content is slightly higher in MVT Py 1 compared to MVT Py 2; this is likely due to the presence of chalcopyrite inclusions in Py 1. Zinc is difficult to compare because most values are at the lower limit of detection (62.7 ppm) in Py 1, and in MVT Py 2 there are outliers with Zn values up to 120 000 ppm alongside correspondingly high (up to 1600 ppm) Cd values (both likely due to sphalerite inclusions or adjacent sphalerite grains). Gold values in Py 1 are very low and near the lower limit of detection (0.056 ppm).

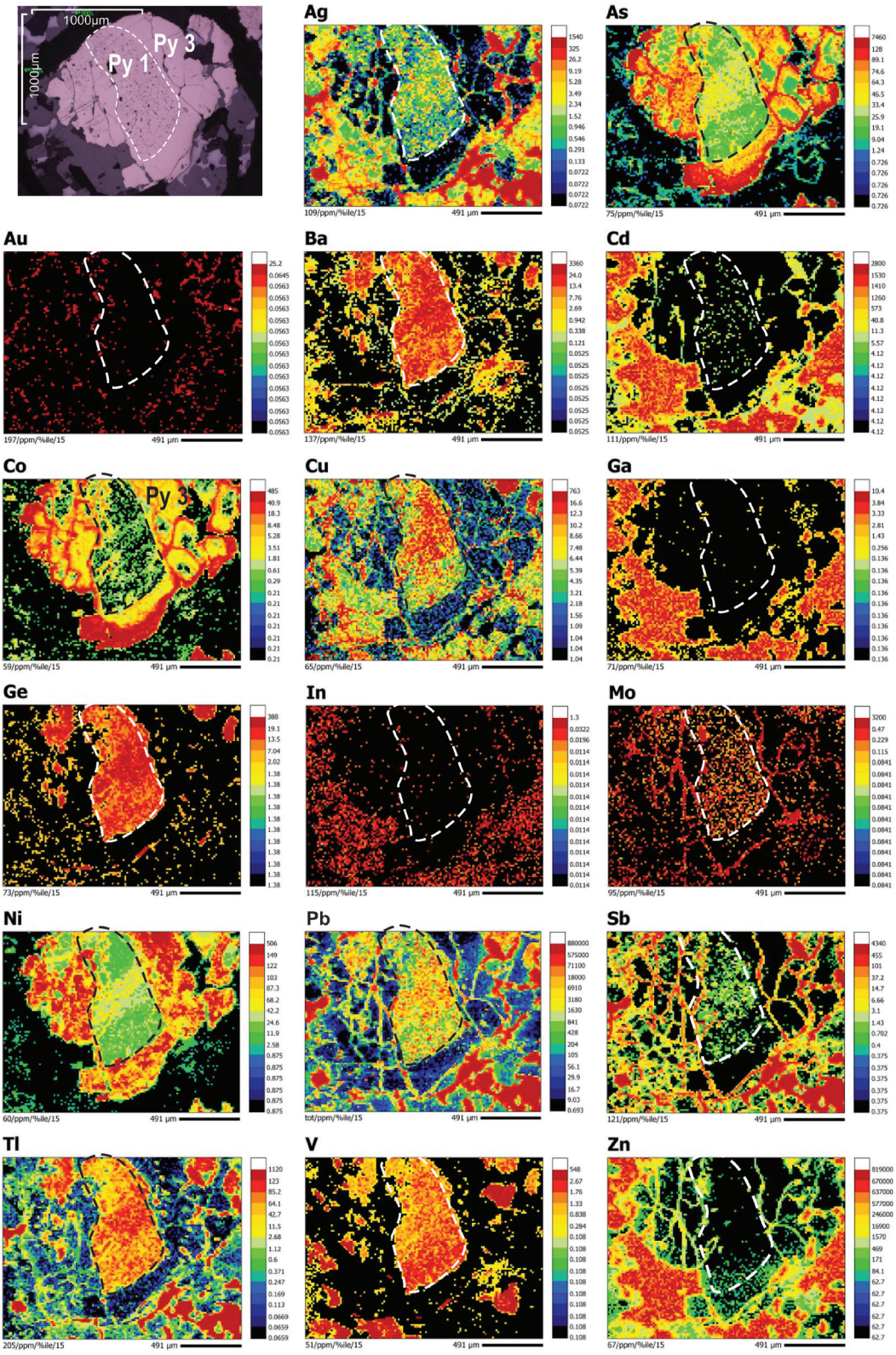

Figure 3. Polished thin section image and laser-ablation inductively coupled plasma mass spectrometry (LA-ICP-MS) distribution maps of trace elements Ag to Zn in pyrite (Py 1 and Py 3) surrounded by sphalerite from sample 08-SP-121 of the Mississippi Valley–type Duncan deposit (no. 1 zone). Pixels are assigned colours based on concentration ranges (in ppm) determined using a percentile scaling function. Gold, cadmium, gallium, indium, and tin (not shown) are all at background levels (black throughout most of the interior of the pyrite grains). Measurement parameters below each map (e.g. 109/ppm/%ile/15) are as follows: 109 = isotopic mass measured (i.e. mass 109 for Ag), ppm = concentration unit, %ile = percentile scaled, 15 = pixel size in microns.

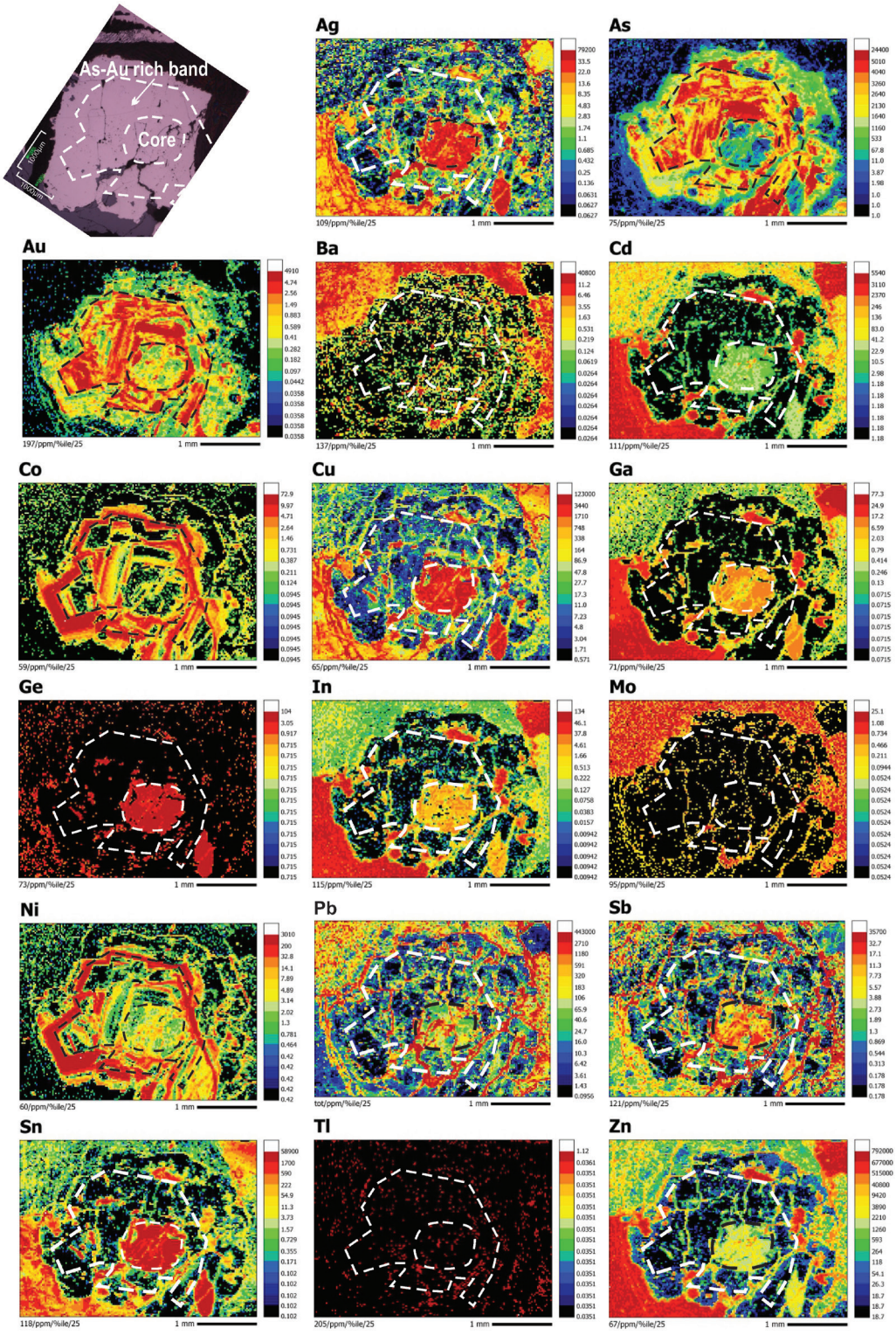

Figure 4. Polished thin section image and laser-ablation inductively coupled plasma mass spectrometry (LA-ICP-MS) distribution maps of trace elements Ag through Zn in pyrite (Py 2) from sample 08-SP-155 of the Abbott-Wagner fracture-controlled replacement deposit. The polished thin section image outlines the enrichment zones within the pyrite grains with a core enriched in Ag, Cu, Ga, Ge, In and Sn; a middle zone with Au- and As-rich bands; and a rim enriched in Co and Ni. Molybdenum, vanadium (not shown), and thallium are at background levels (black throughout most of the interior of the pyrite grains). Pixels are assigned colours based on concentration ranges (in ppm) determined using a percentile scaling function. Measurement parameters below each map (e.g. 109/ppm/%ile/25) are as follows: 109 = isotopic mass measured (i.e. mass 109 for Ag), ppm = concentration unit, %ile = percentile scaled, 25 = pixel size in microns.

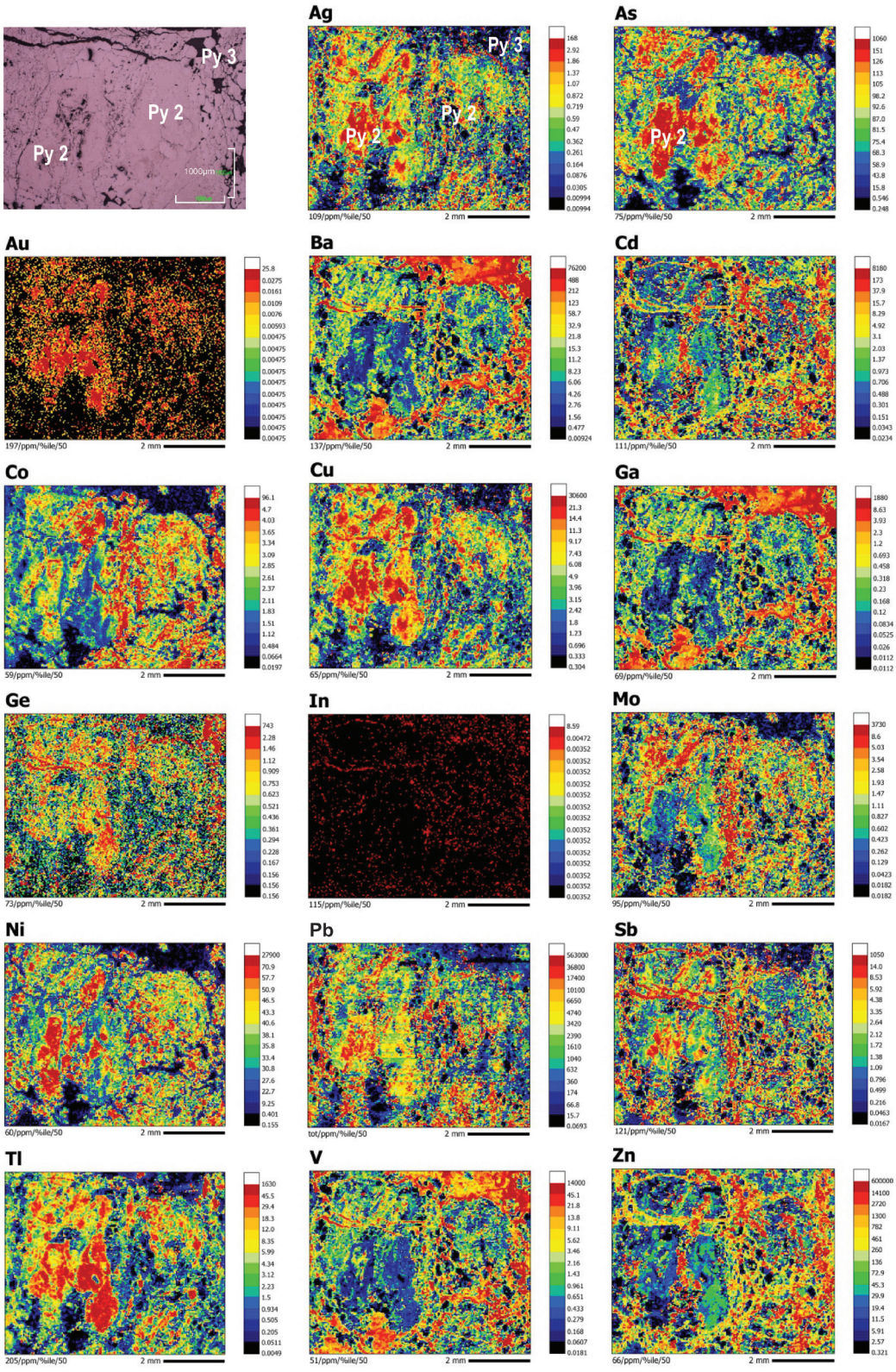

Figure 5. Polished thin section image and laser-ablation inductively coupled plasma mass spectrometry (LA-ICP-MS) distribution maps of trace elements Ag to Zn in pyrite (Py 2 and Py 3) from sample 08-SP-77B of the Reeves MacDonald Mississippi Valley–type deposit. Pixels are assigned colours based on concentration ranges (in ppm) determined using a percentile scaling function. Indium is at or below background levels (black throughout most of the interior of the pyrite grains). Measurement parameters below each map (e.g. 109/ppm/%ile/50) are as follows: 109 = isotopic mass measured (i.e. mass 109 for Ag), ppm = concentration unit, %ile= percentile scaled, 50 = pixel size in microns.

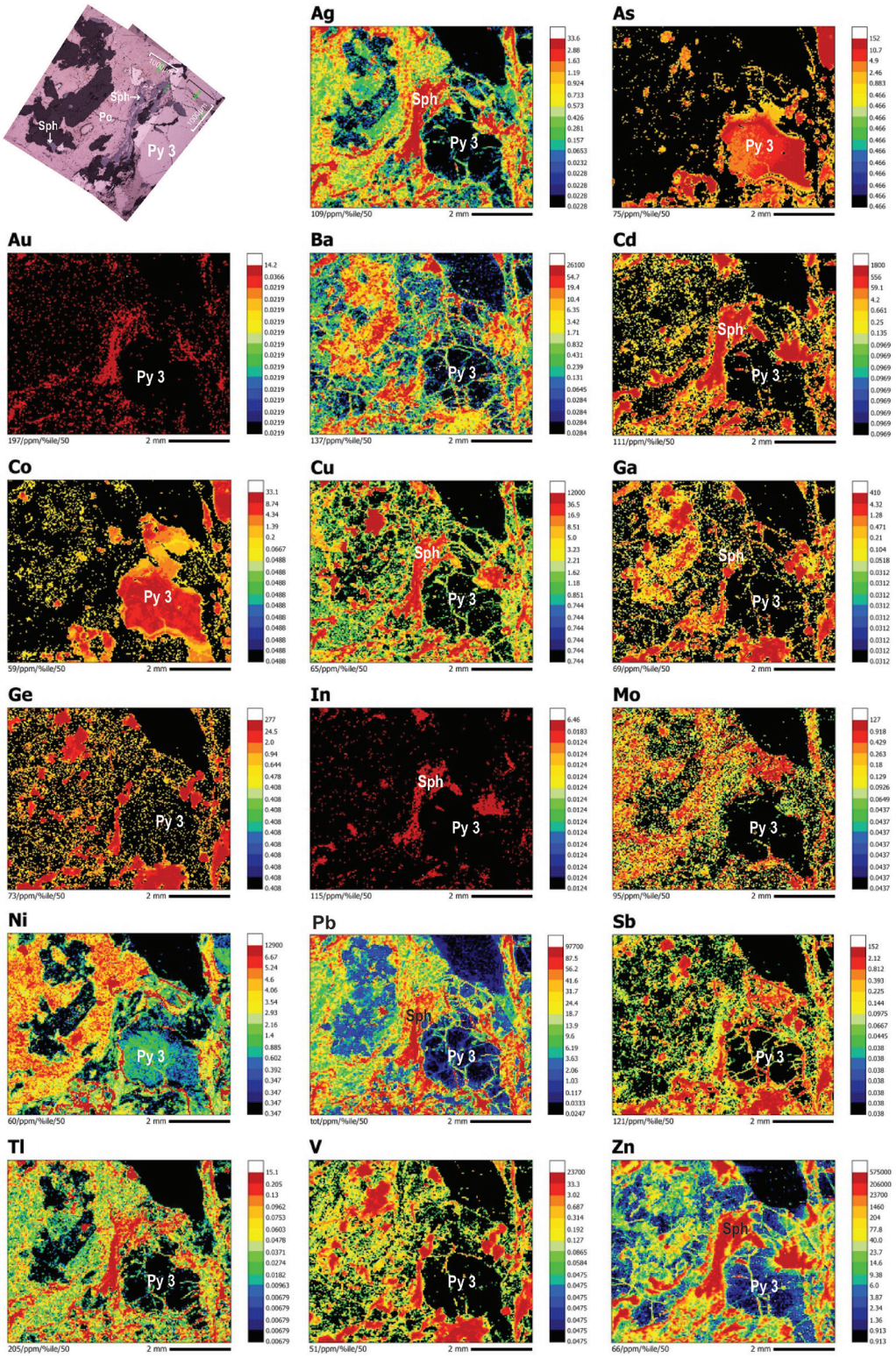

Figure 6. Polished thin section image (slightly offset) and laser-ablation inductively coupled plasma mass spectrometry (LA-ICP-MS) distribution maps of trace elements Ag to Zn in pyrite (Py 3), pyrrhotite, and sphalerite from sample 08-SP-102B of the Jackpot Mississippi Valley–type deposit, Lerwick zone. Pixels are assigned colours based on concentration ranges (in ppm) determined using a percentile scaling function. Silver, gold, barium, cadmium, copper, gallium, germanium, indium, molybdenum, lead, antimony, and thallium are at background levels (black throughout most of the interior of the pyrite grain). Measurement parameters below each map (e.g. 109/ppm/%ile/50) are as follows: 109 = isotopic mass measured (i.e. mass 109 for Ag), ppm = concentration unit, %ile = percentile scaled, 50 = pixel size in microns.

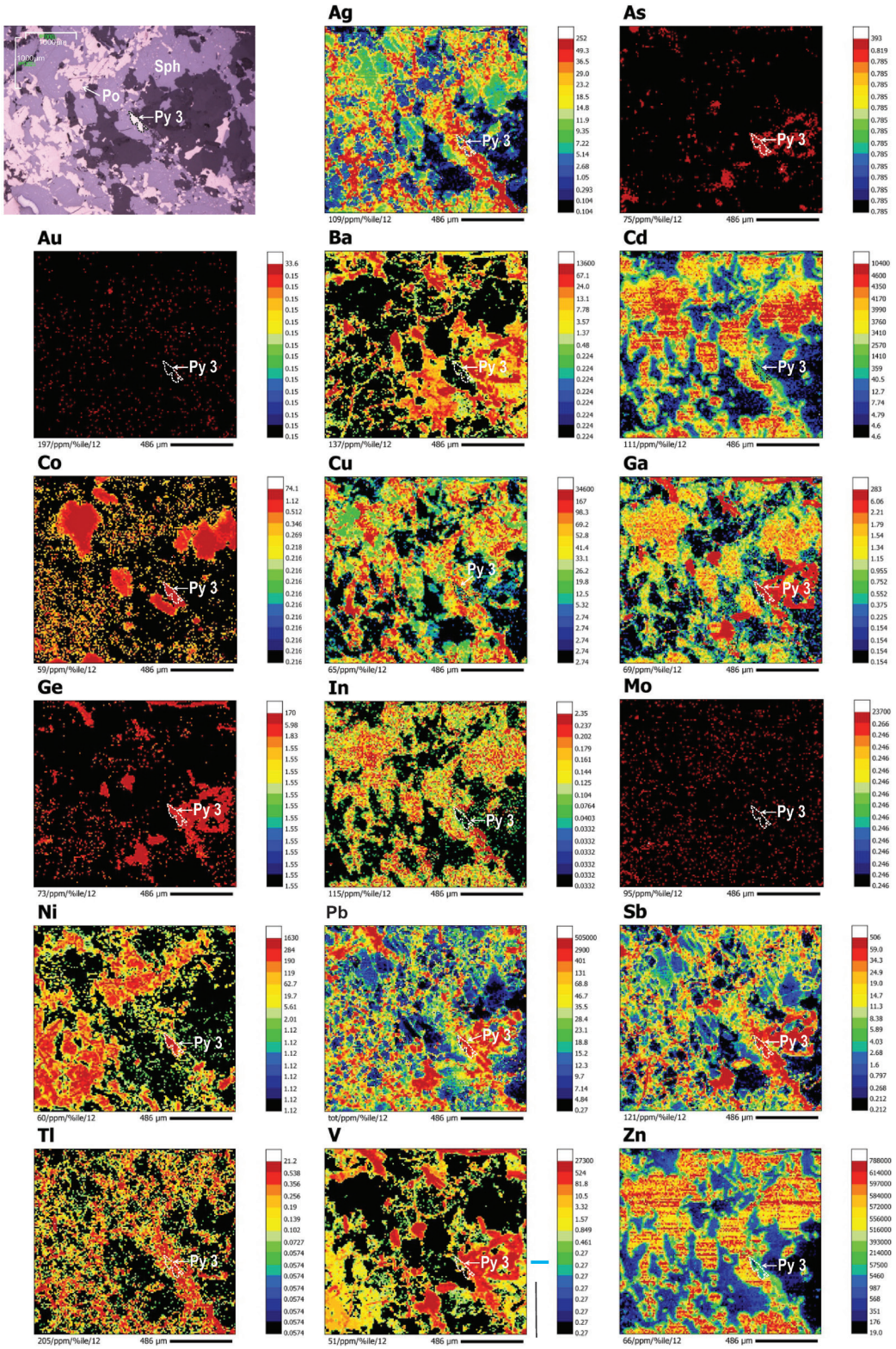

Figure 7. Polished thin section image (lower magnification) and laser-ablation inductively coupled plasma mass spectrometry (LA-ICP-MS) distribution maps of trace elements Ag to Zn in pyrite (Py 3), pyrrhotite, and sphalerite from sample JS-07-56.9 of the Jersey-Emerald Mississippi Valley–type deposit. Arsenic, gold, indium, and molybdenum are at background levels (black throughout most of the interior of the pyrite grain). Pixels are assigned colours based on concentration ranges (in ppm) determined using a percentile scaling function. Measurement parameters below each map (e.g. 109/ppm/%ile/12) are as follows: 109 = isotopic mass measured (i.e. mass 109 for Ag), ppm = concentration unit, %ile = percentile scaled, 12 = pixel size in microns.

Table 2. Summary of trace element composition (ppm) of pyrite in Mississippi Valley–type (MVT) and fracture-controlled replacement (FCR) deposits determined using laser-ablation inductively coupled plasma mass spectrometry (LA-ICP-MS).

	Minimum	Maximum	Mean	Median	Standard deviation	5th percentile	25th percentile	75th percentile	95th percentile
MVT Pyrite 1 (Duncan; n = 559)									
V	0.55	3.7	1.6	1.5	0.45	0.95	1.3	1.9	2.5
Co	0.21	2.8	0.35	0.21	0.29	0.21	0.21	0.36	0.88
Ni	2.8	120	26	24	18	5.8	12	35	58
Cu	1.5	150	13	12	8.8	5.2	8.8	15	23
Zn	63	630	64	63	24	63	63	63	63
Ga	0.14	0.17	0.14	0.14	0.00	0.14	0.14	0.14	0.14
Ge	3.2	50	18	17	5.9	9.0	14	21	28
As	9.3	57	29	29	7.8	16	24	33	43
Se	1.5	6.1	1.6	1.5	0.37	1.5	1.50	1.5	2.0
Mo	0.08	1.9	0.15	0.084	0.17	0.084	0.084	0.12	0.36
Ag	0.07	20	2.6	1.4	3.2	0.210	0.57	3.4	9.5
Cd	4.1	19	4.5	4.1	1.6	4.1	4.1	4.1	7.0
In	0.011	0.018	0.011	0.011	0.001	0.011	0.011	0.011	0.011
Sn	0.22	1.0	0.22	0.22	0.03	0.22	0.22	0.22	0.22
Sb	0.38	11	1.2	0.54	1.6	0.38	0.38	1.4	4.7
Ba	4.2	240	28	19	28	7.8	13	31	84
Au	0.056	1.6	0.059	0.056	0.063	0.056	0.056	0.056	0.056
Tl	18	180	78	75	26	37	59	95	120
Pb	140	210000	20000	7800	29000	560	2400	26000	77000
MVT Pyrite 2 (Reeves MacDonald; n = 1972)									
V	0.018	220	1.5	0.33	8.3	0.061	0.21	0.67	4.9
Co	0.13	10	2.2	1.90	1.3	0.78	1.3	2.7	4.3
Ni	14	210	41	36	19	23	30	45	76
Cu	0.30	69	12	11	9.3	1.40	7.1	15	32
Zn	0.32	120000	730	36	5100	2.20	19	60	1800
Ga	0.01	26	0.22	0.081	0.76	0.011	0.034	0.19	0.77
Ge	0.16	19	1.0	0.87	0.94	0.16	0.50	1.3	2.3
As	9.4	450	120	110	52	68	92	130	230
Se	0.22	20	0.68	0.44	0.97	0.22	0.23	0.76	1.8
Mo	0.018	310	2.2	0.81	10	0.057	0.47	1.6	6.4
Ag	0.010	7	1.1	0.78	1.0	0.094	0.49	1.3	3.4
Cd	0.023	1600	9.4	0.93	64	0.057	0.55	1.7	23
In	0.004	0.013	0.004	0.004	0.000	0.004	0.004	0.004	0.004
Sn	0.037	1.4	0.040	0.037	0.048	0.037	0.037	0.037	0.037

Table 2 (cont.). Summary of trace element composition (ppm) of pyrite in Mississippi Valley–type (MVT) and fracture-controlled replacement (FCR) deposits determined using laser-ablation inductively coupled plasma mass spectrometry (LA-ICP-MS).

	Minimum	Maximum	Mean	Median	Standard deviation	5th percentile	25th percentile	75th percentile	95th percentile
Sb	0.017	87	2.5	1.7	3.30	0.25	1.1	2.9	6.7
Ba	0.009	1200	13	4.5	44	0.50	2.3	10	44
Au	0.005	0.19	0.019	0.010	0.024	0.005	0.005	0.021	0.068
Tl	0.005	100	36	39	22	0.62	16	52	69
Pb	0.069	160000	6200	4100	11000	120	2100	6500	17000
MVT Pyrite 3 (Duncan; n = 318)									
V	0.11	1.6	0.13	0.11	0.12	0.11	0.11	0.11	0.15
Co	0.21	42	4.6	4.3	3.7	0.46	3.2	5.6	8.3
Ni	47	360	160	150	59	89	120	190	280
Cu	1.0	24	1.9	1.1	2.2	1.0	1.0	1.9	5.2
Zn	63	1600	68	63	86	63	63	63	63
Ga	0.14	0.17	0.14	0.14	0.002	0.14	0.14	0.14	0.14
Ge	1.40	14	1.6	1.4	1.2	1.4	1.4	1.4	1.7
As	6.50	130	58	65	25	10	48	75	88
Se	1.50	1.7	1.5	1.5	0.009	1.5	1.5	1.5	1.5
Mo	0.084	1.1	0.091	0.084	0.064	0.084	0.084	0.084	0.084
Ag	0.072	2.5	0.13	0.07	0.24	0.072	0.072	0.072	0.33
Cd	4.10	16	4.2	4.1	0.76	4.1	4.1	4.1	4.1
In	0.011	0.019	0.011	0.011	0.001	0.011	0.011	0.011	0.011
Sn	0.22	0.22	0.22	0.22	0.000	0.22	0.22	0.22	0.22
Sb	0.38	2.5	0.38	0.38	0.13	0.38	0.38	0.38	0.38
Ba	0.053	23	0.27	0.053	1.5	0.053	0.053	0.053	1.0
Au	0.056	0.056	0.056	0.056	0.000	0.056	0.056	0.056	0.056
Tl	0.066	92	2.20	0.069	9.5	0.066	0.066	0.200	13
Pb	1.10	22000	270	36	1500	4.0	13	91	550
MVT Pyrite 3 (Jersey-Emerald; n = 44)									
V	0.27	340	16	0.44	52	0.27	0.27	14	53
Co	11	68	26	23	15	11	15	32	63
Ni	140	1400	550	540	270	180	320	690	1100
Cu	2.7	420	22	5.80	66	2.7	2.8	8.9	110
Zn	97	140000	30000	26000	30000	120	4000	41000	100000
Ga	0.15	1.2	0.20	0.15	0.17	0.15	0.15	0.16	0.39
Ge	1.6	1.6	1.6	1.6	0.000	1.6	1.6	1.6	1.6
As	0.79	390	38	6.1	79	0.79	1.9	23	240
Se	2.5	37	13	13	6.4	3.0	8.8	16	24

Table 2 (cont.). Summary of trace element composition (ppm) of pyrite in Mississippi Valley–type (MVT) and fracture-controlled replacement (FCR) deposits determined using laser-ablation inductively coupled plasma mass spectrometry (LA-ICP-MS).

	Minimum	Maximum	Mean	Median	Standard deviation	5th percentile	25th percentile	75th percentile	95th percentile
Mo	0.25	0.61	0.26	0.25	0.06	0.25	0.25	0.25	0.34
Ag	0.10	66	15	10	15	0.10	4.1	19	60
Cd	4.6	1100	210	160	220	4.6	29	300	700
In	0.033	0.079	0.036	0.033	0.009	0.033	0.033	0.033	0.068
Sn	0.26	8.6	1.20	0.33	1.9	0.26	0.26	1.3	6.3
Sb	0.21	96	26	19	24	0.35	6.5	38	87
Ba	0.22	12	0.99	0.22	2.0	0.22	0.22	0.66	4.8
Au	0.15	0.43	0.16	0.15	0.047	0.15	0.15	0.15	0.27
Tl	0.057	1.2	0.27	0.23	0.26	0.057	0.069	0.34	1.0
Pb	2.6	40 000	3000	190	7700	3.6	27	1900	26 000
MVT Pyrite 3 (Jackpot-Lerwick; n = 5537)									
V	0.047	2200	1.7	0.047	41	0.047	0.047	0.047	0.46
Co	0.049	25	6.1	6.5	4.3	0.28	2.0	9.2	13
Ni	0.35	91	2.7	0.84	5.9	0.35	0.51	1.9	12
Cu	0.74	1600	2.2	0.74	23	0.74	0.74	1.1	5.2
Zn	0.91	33 000	480	4.3	2600	0.91	1.7	19	1200
Ga	0.031	43	0.21	0.031	1.4	0.031	0.031	0.031	0.49
Ge	0.41	94	0.83	0.41	3.9	0.41	0.41	0.41	1.0
As	0.47	130	7.1	4.7	8.8	0.47	1.0	9.9	25
Se	0.38	1.0	0.39	0.38	0.036	0.38	0.38	0.38	0.38
Mo	0.044	30	0.26	0.044	0.91	0.044	0.044	0.068	1.2
Ag	0.023	6.5	0.15	0.023	0.34	0.023	0.023	0.10	0.78
Cd	0.10	100	1.5	0.10	7.5	0.097	0.10	0.10	4.0
In	0.012	0.094	0.013	0.012	0.002	0.012	0.012	0.012	0.012
Sn	0.090	24	0.11	0.090	0.37	0.090	0.090	0.090	0.090
Sb	0.038	27	0.53	0.051	1.2	0.038	0.038	0.42	2.5
Ba	0.028	5300	8.6	0.060	99	0.028	0.028	0.74	17
Au	0.022	0.40	0.022	0.022	0.006	0.022	0.022	0.022	0.022
Tl	0.007	2.1	0.055	0.007	0.12	0.007	0.007	0.052	0.24
Pb	0.025	14 000	29	1.1	330	0.025	0.056	10	66
FCR Pyrite 2 (Abbott-Wagner; n = 11 164)									
V	0.057	74	0.49	0.057	2.6	0.057	0.057	0.057	1.8
Co	0.10	73	3.6	0.83	6.3	0.095	0.10	4.0	18
Ni	0.42	3000	93	4.8	280	0.42	1.1	24	590
Cu	0.57	120 000	620	13	2500	1.1	4.0	120	3700

Table 2 (cont.). Summary of trace element composition (ppm) of pyrite in Mississippi Valley–type (MVT) and fracture-controlled replacement (FCR) deposits determined using laser-ablation inductively coupled plasma mass spectrometry (LA-ICP-MS).

	Minimum	Maximum	Mean	Median	Standard deviation	5th percentile	25th percentile	75th percentile	95th percentile
Zn	19	330000	6500	74	29000	19	19	1400	26000
Ga	0.071	77	1.2	0.071	2.8	0.071	0.071	0.30	8.2
Ge	0.72	23	1.5	0.72	2.4	0.72	0.72	0.72	7.4
As	1.00	24000	2700	2400	1900	23	1300	3900	6000
Se	0.88	23	0.96	0.88	0.37	0.88	0.88	0.88	1.4
Mo	0.052	25	0.073	0.052	0.26	0.052	0.052	0.052	0.15
Ag	0.063	5400	8.8	0.88	90.00	0.063	0.19	4.4	35
Cd	1.2	2000	33	1.2	140	1.2	1.2	9.2	120
In	0.009	54	0.91	0.011	2.6	0.009	0.009	0.25	5.0
Sn	0.10	36000	290	0.18	860	0.10	0.10	7.8	2300
Sb	0.18	36000	13	1.1	440	0.18	0.25	5.3	22
Ba	0.026	1300	1.4	0.026	24	0.026	0.026	0.13	1.7
Au	0.036	160	2.7	0.67	8.7	0.051	0.27	2.2	8.9
Tl	0.035	0.45	0.059	0.047	0.04	0.036	0.040	0.066	0.12
Pb	0.096	150000	530	23	4200	0.49	5.2	120	1700
FCR Pyrite 3 (Abbott-Wagner; n = 473)									
V	0.057	1.3	0.064	0.057	0.066	0.057	0.057	0.057	0.058
Co	0.10	86	18	17	15	1.7	5.5	23	50
Ni	0.42	3100	690	430	750	2.8	79	1100	2300
Cu	0.57	1700	14	2.5	88	0.57	1.1	5.9	35
Zn	19	260000	2300	40	16000	19	21	100	4200
Ga	0.071	7.8	0.15	0.071	0.50	0.071	0.071	0.085	0.31
Ge	0.72	1.2	0.72	0.72	0.033	0.72	0.72	0.72	0.74
As	9.7	5100	1700	1600	590	1000	1400	2000	2700
Se	0.88	1.6	0.92	0.88	0.076	0.88	0.88	0.90	1.0
Mo	0.052	0.98	0.066	0.052	0.054	0.052	0.052	0.085	0.094
Ag	0.049	11	0.65	0.13	1.5	0.049	0.063	0.53	3.2
Cd	1.2	1400	14	1.20	84	1.200	1.2	3.0	39
In	0.009	15	0.16	0.009	0.97	0.009	0.009	0.016	0.44
Sn	0.10	200	2.5	0.10	15	0.10	0.10	0.15	4.9
Sb	0.18	17	0.87	0.21	1.8	0.18	0.18	0.70	3.5
Ba	0.026	54	0.44	0.026	2.9	0.026	0.026	0.053	1.3
Au	0.036	4.3	0.55	0.43	0.54	0.053	0.26	0.67	1.2
Tl	0.035	0.18	0.038	0.035	0.009	0.035	0.035	0.035	0.045
Pb	0.10	3800	53	2.5	250	0.10	0.46	13	220

Abbreviations: MVT: Mississippi Valley–type; FCR: fracture-controlled replacement.

Table 3. Various trace element ratios of pyrite in Mississippi Valley–type (MVT) and fracture-controlled replacement (FCR) deposits determined using laser-ablation inductively coupled plasma mass spectrometry (LA-ICP-MS).

	Ni-Co	Co-Ni	Ag-Ni	Zn-Ni	Tl-Co	Tl-Sb	Tl-As	As-Au	Au-Ag
MVT Pyrite 1 (Duncan; n = 559)									
Minimum	9.8	0.002	0.004	0.51	14	11	0.82	22	0.003
Maximum	580	0.10	2.3	100	860	340	7.7	1000	0.78
Mean	93	0.018	0.14	4.0	290	120	2.8	510	0.077
Median	76	0.013	0.064	2.6	290	110	2.7	510	0.043
Standard deviation	71	0.015	0.23	5.2	150	71	0.96	140	0.10
5th percentile	22	0.005	0.010	1.1	71	22	1.5	280	0.006
25th percentile	41	0.008	0.027	1.8	180	56	2.2	420	0.017
75th percentile	130	0.024	0.15	5.1	390	170	3.3	590	0.099
95th percentile	210	0.046	0.54	11	560	240	4.6	760	0.27
MVT Pyrite 2 (Reeves MacDonald; n = 1972)									
Minimum	3.9	0.003	0	0.003	0.003	0.031	0	980	0.001
Maximum	350	0.26	0.22	6800	300	99	0.97	56000	0.48
Mean	23	0.054	0.028	20	25	20	0.30	12000	0.029
Median	20	0.051	0.023	0.99	17	17	0.30	11000	0.016
Standard deviation	14	0.025	0.022	190	27	15	0.20	7600	0.065
5th percentile	11	0.023	0.002	0.046	0.29	1.2	0.008	2900	0.005
25th percentile	15	0.037	0.013	0.48	5.90	7.2	0.14	5400	0.009
75th percentile	27	0.067	0.038	1.7	35	29	0.44	18000	0.025
95th percentile	43	0.094	0.071	50	75	49	0.63	24000	0.064
MVT Pyrite 3 (Duncan; n = 318)									
Minimum	2.4	0.001	0	0.17	0.002	0.18	0.001	120	0.022
Maximum	720	0.42	0.048	13	72	250	3.1	2400	0.78
Mean	71	0.033	0.001	0.48	0.94	5.7	0.054	1000	0.69
Median	37	0.027	0.001	0.43	0.021	0.18	0.001	1100	0.78
Standard deviation	720	0.037	0.003	0.72	5.2	25	0.27	440	0.76
5th percentile	15	0.003	0	0.22	0.009	0.18	0.001	180	0.17
25th percentile	29	0.020	0	0.32	0.015	0.18	0.001	850	0.78
75th percentile	50	0.035	0.001	0.52	0.066	0.52	0.008	1300	0.78
95th percentile	310	0.068	0.002	0.74	4.0	34	0.19	1600	0.78
MVT Pyrite 3 (Jersey-Emerald; n = 44)									
Minimum	2.5	0.017	0	0.16	0.001	0.003	0	5.2	0.002
Maximum	59	0.40	0.20	400	0.071	0.27	0.35	2600	1.4
Mean	27	0.072	0.035	79	0.013	0.027	0.060	240	0.12
Median	27	0.037	0.020	46	0.009	0.011	0.035	37	0.015

Table 3 (cont.). Various trace element ratios of pyrite in Mississippi Valley–type (MVT) and fracture-controlled replacement (FCR) deposits determined using laser-ablation inductively coupled plasma mass spectrometry (LA-ICP-MS).

	Ni-Co	Co-Ni	Ag-Ni	Zn-Ni	Tl-Co	Tl-Sb	Tl-As	As-Au	Au-Ag
Standard deviation	15	0.087	0.043	97	0.013	0.056	0.078	520	0.36
5th percentile	3	0.017	0	0.18	0.001	0.004	0.001	5.2	0.003
25th percentile	16	0.028	0.006	7.0	0.004	0.008	0.006	13	0.009
75th percentile	36	0.064	0.044	100	0.016	0.016	0.073	140	0.037
95th percentile	58	0.34	0.14	330	0.037	0.230	0.27	1600	1.4
MVT Pyrite 3 (Jackpot-Lerwick; n = 5537)									
Minimum	0.028	0.001	0.001	0.040	0	0.001	0	5.9	0.006
Maximum	1000	36	4.9	75000	8.4	14	2.2	6100	1.4
Mean	3.4	8.1	0.070	300	0.075	0.21	0.044	320	0.68
Median	0.14	7.4	0.042	4.4	0.003	0.18	0.003	210	0.96
Standard deviation	21	7.2	0.12	2500	0.32	0.36	0.12	400	0.39
5th percentile	0.047	0.074	0.012	0.66	0.001	0.027	0	21	0.030
25th percentile	0.075	1.0	0.026	1.9	0.001	0.10	0.001	45	0.23
75th percentile	0.97	13	0.066	16	0.022	0.18	0.025	450	0.96
95th percentile	13	21	0.21	530	0.32	0.51	0.23	1100	0.96
FCR Pyrite 2 (Abbott-Wagner; n = 11 164)									
Minimum	0.10	0.001	0	0.006	0	0	0	0.97	0
Maximum	710	11	2200	760 000	1.8	1.0	0.035	180 000	2300
Mean	18	0.30	3.200	2200	0.14	0.071	0	7600	9.0
Median	6.9	0.14	0.19	44	0.044	0.031	0	2500	0.74
Standard deviation	29	0.57	34.000	19 000	0.16	0.078	0.002	15 000	53
5th percentile	0.83	0.016	0.001	0.082	0.002	0.002	0	53	0.012
25th percentile	3.7	0.047	0.023	3.2	0.009	0.007	0	750	0.16
75th percentile	21	0.27	1.4	280	0.37	0.140	0	7300	3.5
95th percentile	62	1.2	13	3700	0.37	0.200	0.002	32 000	34
FCR Pyrite 3 (Abbott-Wagner; n = 473)									
Minimum	0.15	0.005	0	0.006	0	0.002	0	270	0.011
Maximum	190	6.9	0.93	1700	0.37	1.0	0.004	65 000	52
Mean	32	0.24	0.022	18	0.009	0.14	0	6200	4.3
Median	28	0.036	0.001	0.17	0.002	0.20	0	3600	2.5
Standard deviation	25	0.79	0.083	110	0.027	0.087	0	8300	5.2
5th percentile	1.2	0.013	0	0.013	0.001	0.010	0	1200	0.12
25th percentile	13	0.022	0	0.047	0.002	0.053	0	2400	0.69
75th percentile	46	0.078	0.006	2.2	0.007	0.20	0	6200	6.6
95th percentile	75	0.84	0.14	50	0.021	0.21	0	24 000	12

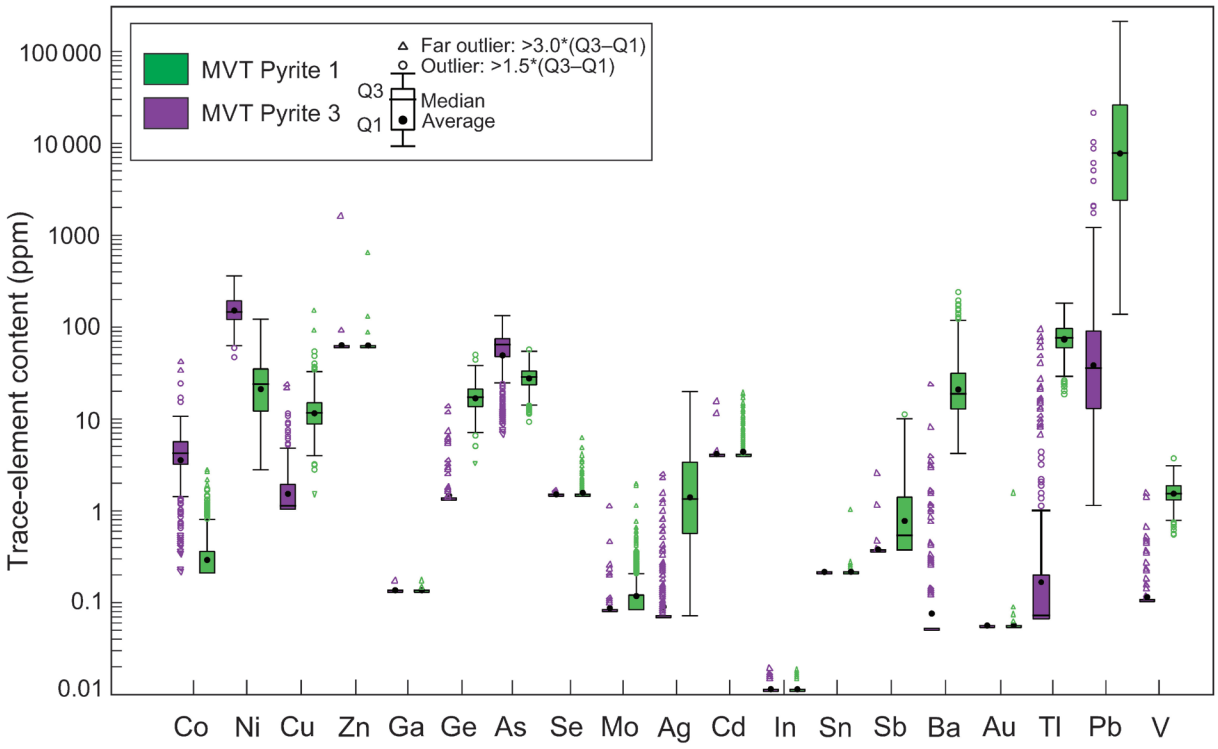

Figure 8. Box and whisker plots of trace-element content for Pyrite 1 and Pyrite 3 from the Duncan deposit (sample 08-SP-121). Except for V, elements are listed from left to right in order of increasing atomic number and atomic weight. Concentrations span seven orders of magnitude. Symbols: Q3 = top of box; Q1 = bottom of box; black circle = average; line = median. The central box is the middle 50% of the data from Q1 to Q3. An outlier (circle) is further than 1.5 × (Q3–Q1) from the box. A far outlier (triangle) is further than 3.0 × (Q3–Q1) from the box. The whiskers are the extreme values that are not outliers.

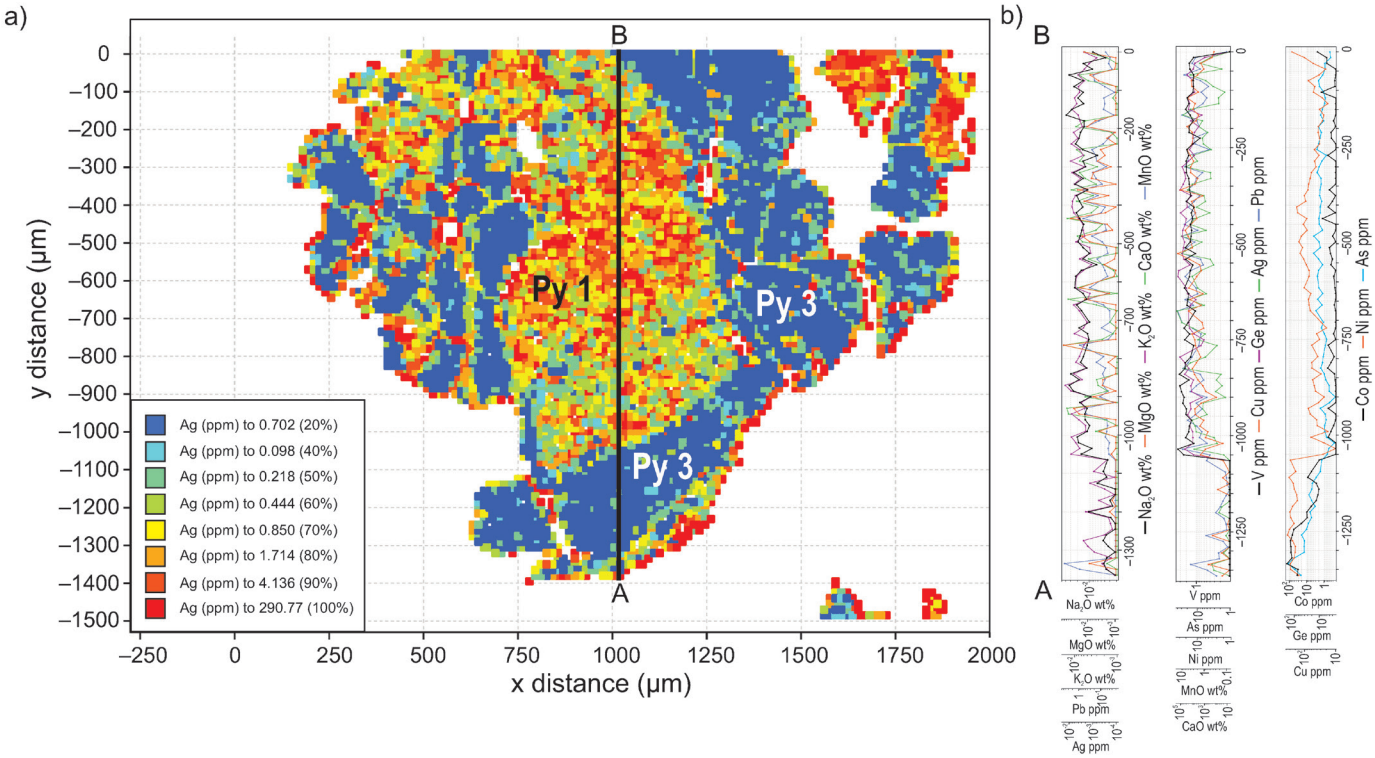

Figure 9. **a)** Laser-ablation inductively coupled plasma mass spectrometry (LA-ICP-MS) Ag distribution map of pyrite from sample 08-SP-121 from the Duncan no. 1 zone, generated with ioGAS, and **b)** trace-element profiles along a linear transect (black line A–B). Pixels are assigned colours based on concentration ranges (in ppm) determined from the LA-ICP-MS data.

Pyrite 2

The main metallogenic elements — Ag, Au, Cd, Cu, Sb, Sn, and Zn — are higher in FCR Py 2 than in MVT Py 2 (Fig. 10; Table 2). Relative to FCR Py 2, Py 2 in MVT deposits is enriched in Ba, Co, Mo, Ni, Tl, and Pb and depleted in all the other elements determined. The contents of Cu, Zn, Ag, and Au in MVT Py 2 are substantially lower than in FCR Py 2, and although Pb in MVT Py 2 is higher overall, it has similar ranges of values in both deposit types due to abundant outliers in both the low and high ranges. The Ga content ranges from 0.01 to 26 ppm in MVT Py 2 and from 0.07 to 77 ppm in FCR Py 2. The ranges of Ge values in both deposit types are similar (0.16–19 ppm in MVT and 0.72–23 ppm in FCR). Indium content in MVT Py 2 is close to the lower limit of detection (0.007 ppm), and ranges from 0.01 to 54 ppm in FCR deposit. Gallium, germanium, and indium contents are highest in Cu-rich zones of the FCR Py 2. Thallium is much lower in FCR Py 2 (0.04–0.45 ppm) than in MVT Py 2 (0.01–100 ppm).

One of the most striking observations is the substantial enrichment of Au and As in FCR Py 2 relative to MVT Py 2. Gold and arsenic in MVT Py 2 range from 0.005 to 0.19 ppm (median 0.01) and 9.4 to 450 ppm (median 109), respectively. Gold and arsenic values can reach up to 160 ppm (median 0.7 ppm) and 24 000 ppm (median 2400 ppm), respectively, in FCR Py 2 (i.e. the Abbott-Wagner deposit). The median value of As in FCR Py 2 is low because of numerous outliers between 1.0 and 270 ppm (lower whisker on Fig. 10). Two grains of Py 2 in the Abbott-Wagner FCR deposit were mapped by LA-ICP-MS and have similar trace-element distributions to each other. Element zoning is observed from core to rim, with the cores enriched in Ag, Cu, Ga, Ge, In, Sn, and Zn, followed by bands rich in Au and As, and rims enriched in Co and Ni (Fig. 4). A lateral profile of elements plotted across one of the pyrite grain illustrates these trends (Fig. 11). In these grains, there is good correlation ($R^2 > 0.6$) of Cu-Ag, Cd-Zn, Cu-Sn, and Ga-In (Fig. 12a, b, c, and d, respectively), and moderately good correlation ($R^2 = 0.5–0.6$) between Co and Ni, Ga and Ge, Zn and In, Ag and In, Cu and In, Ag and Sb, Cu and Ga, Ag and Ga, Cu and Sb, and Sb and Pb (Fig. 12e, f, g, h, i, j, k, l, m, and n, respectively). Copper appears to be correlated with Ag and Sn (±Ga, ±In). It is highest in the core of the pyrite grains and along fractures. This suggests that at low levels, Cu probably occurs in the pyrite crystal lattice and at high levels it is evenly

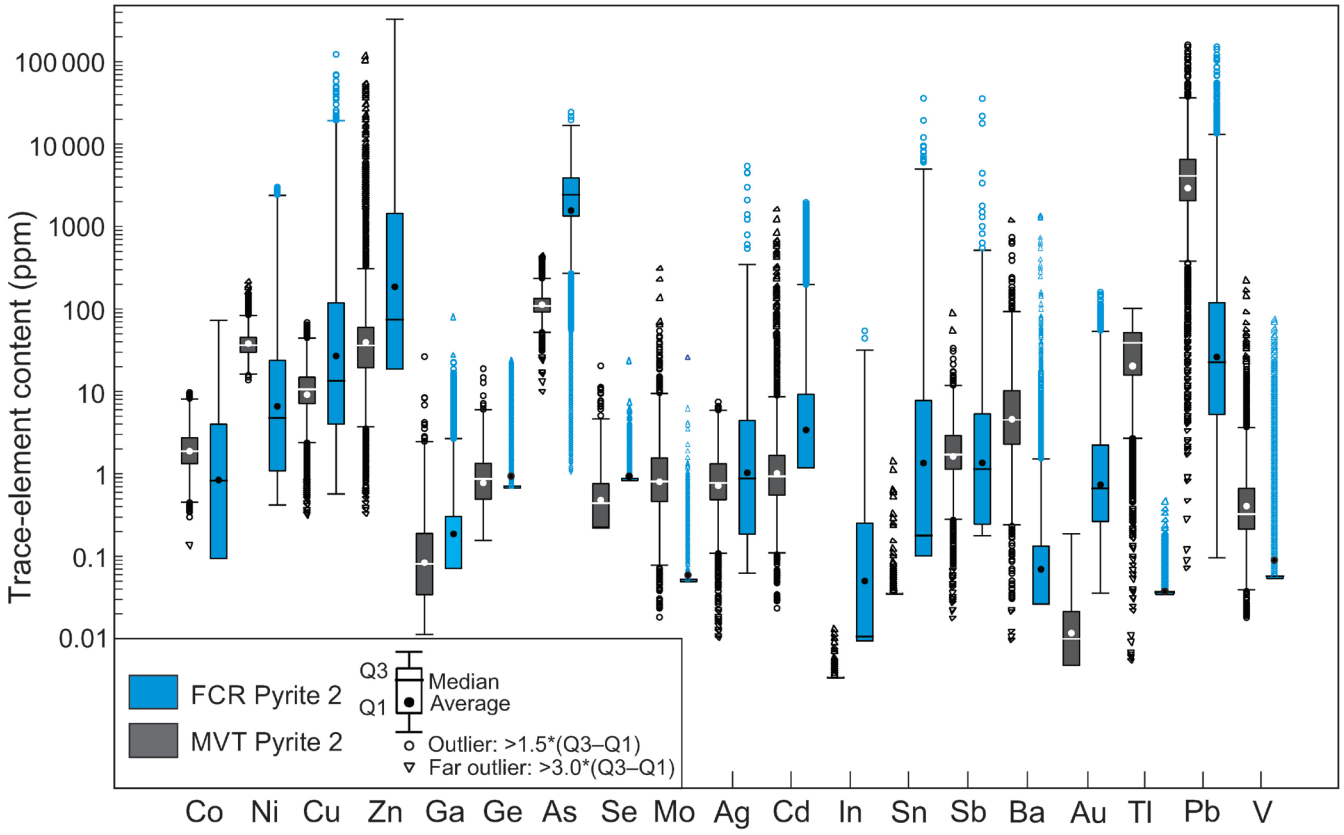

Figure 10. Box and whisker plots of trace-element contents of Pyrite 2 in Mississippi Valley–type and fracture-controlled replacement deposits. Except for V, elements follow are listed from left to right in order of increasing atomic number and atomic weight. Concentrations span eight orders of magnitude. Symbols: Q3 = top of box; Q1 = bottom of box; black circle = average; line = median. The central box is the middle 50% of the data from Q1 to Q3. An outlier (circle) is further than 1.5 × (Q3–Q1) from the box. A far outlier (triangle) is further than 3.0 × (Q3–Q1) from the box. The whiskers are the extreme values that are not outliers.

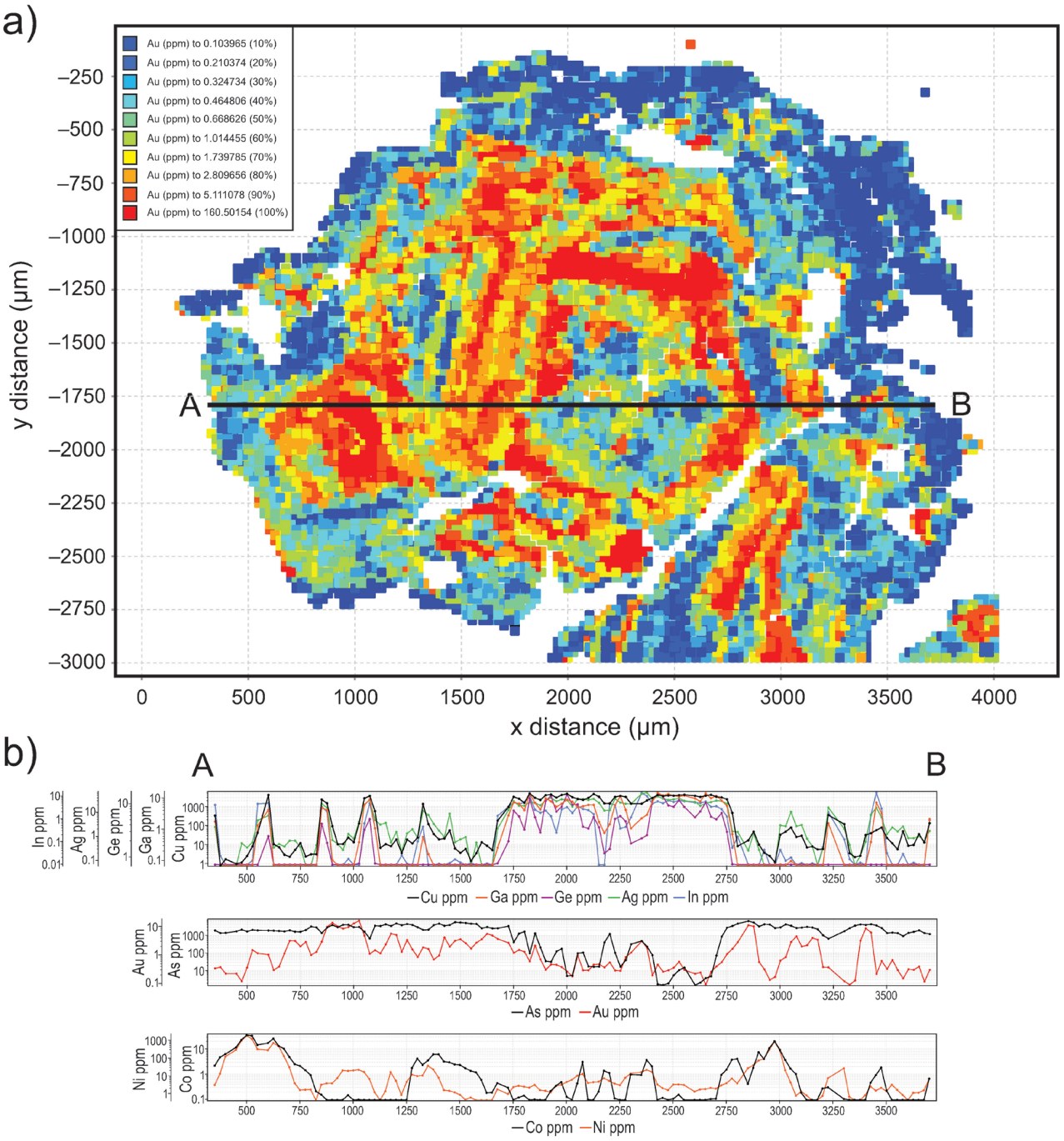

Figure 11. **a)** Laser-ablation inductively coupled plasma mass spectrometry (LA-ICP-MS) Au distribution map of a pyrite grain in sample 08-SP-155 from the Abbott-Wagner deposit, generated with ioGAS, and **b)** trace-element profiles along a linear transect (black line A–B). Pixels are assigned colours based on concentration ranges (in ppm) determined from the LA-ICP-MS data.

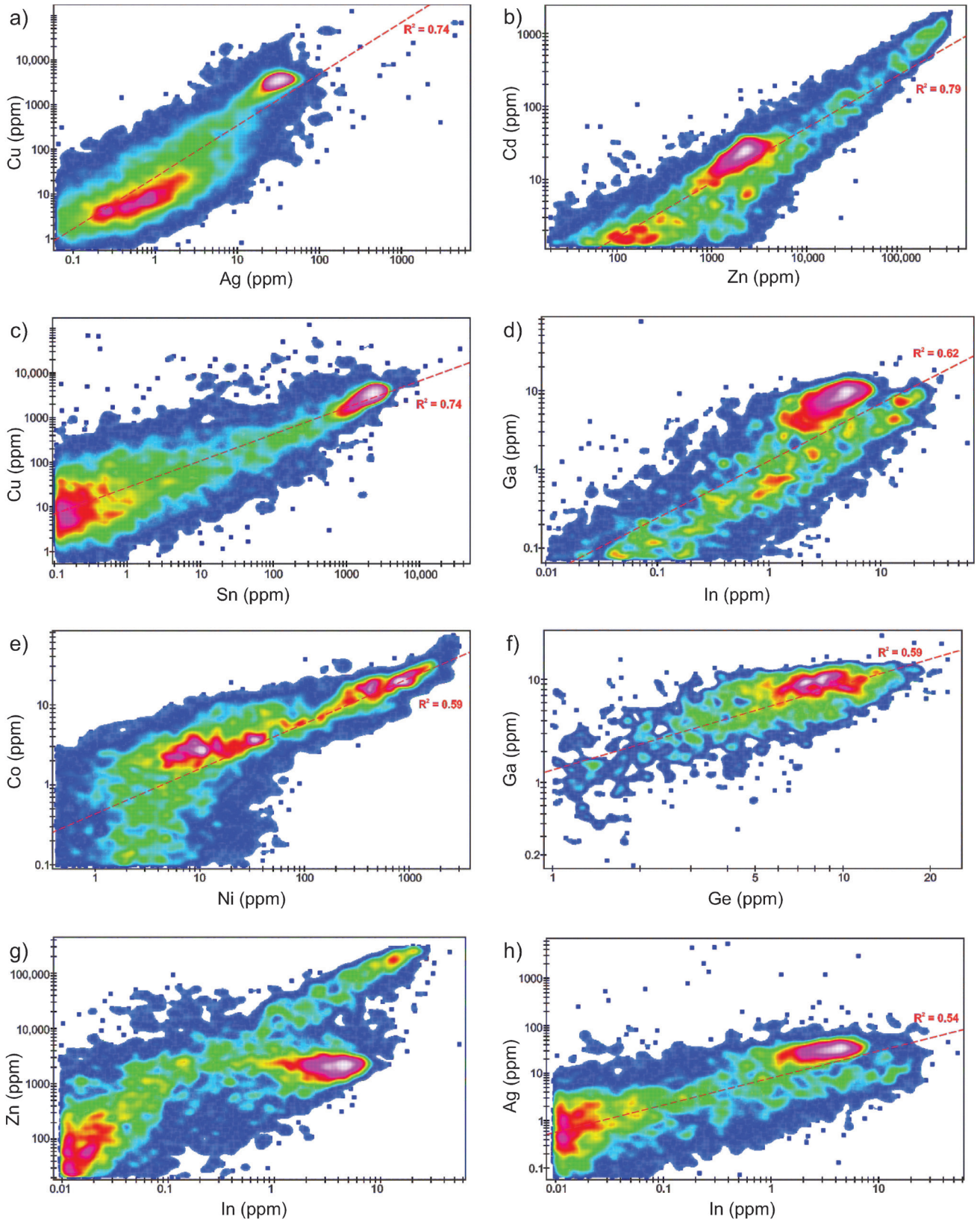

Figure 12. Binary plots of laser-ablation inductively coupled plasma mass spectrometry (LA-ICP-MS) data for pairs of trace elements with high to low levels of covariance throughout Pyrite 2 from sample 08-SP-155 from the Abbott-Wagner fracture-controlled replacement deposit. The variation of colours from blue to pink corresponds to an increase in point density: **a)** Cu vs. Ag; **b)** Cd vs. Zn; **c)** Cu vs. Sn; **d)** Ga vs. In; **e)** Co vs. Ni; **f)** Ga vs. Ge; **g)** Zn vs. In; **h)** Ag vs. In.

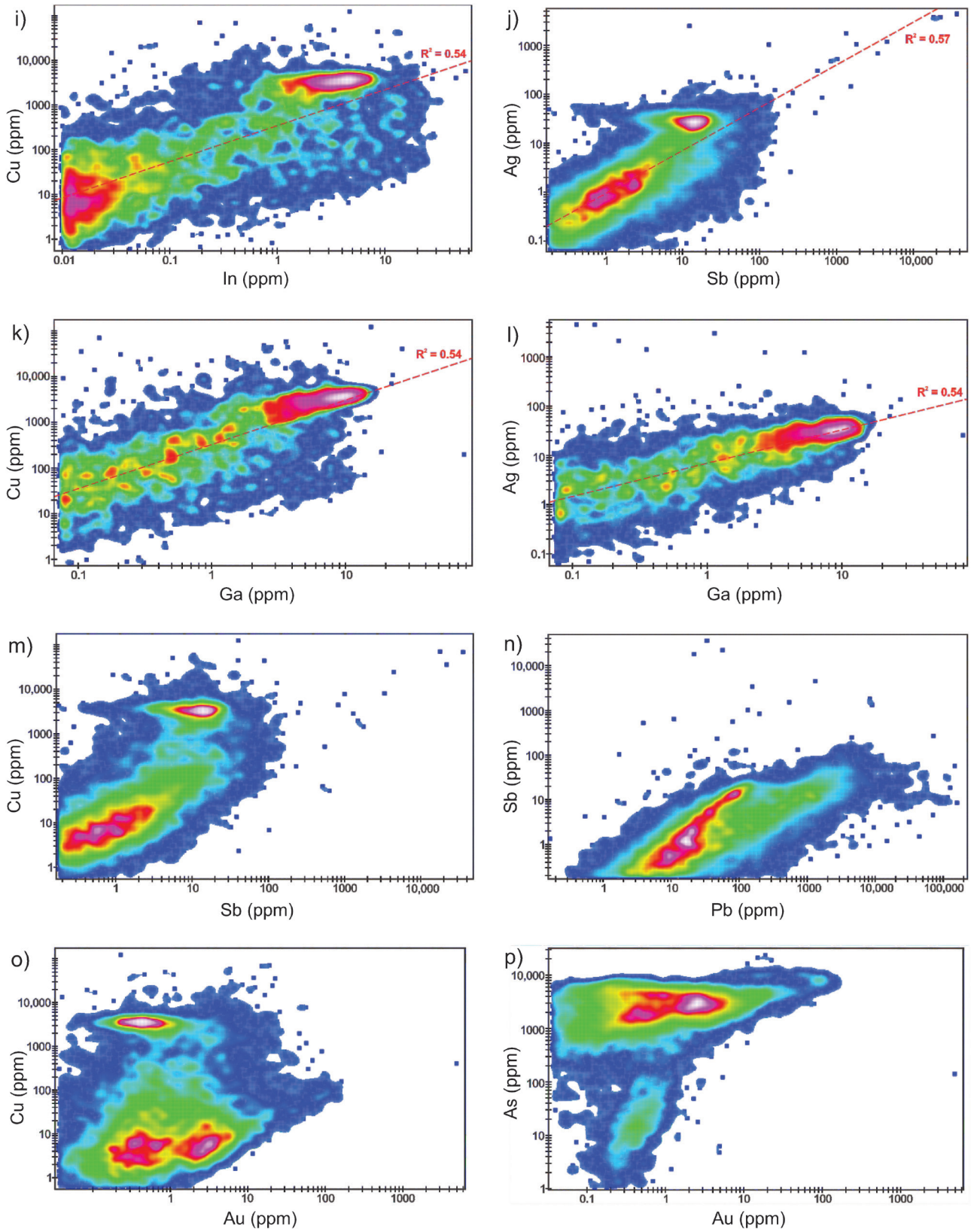

Figure 12 (cont.). Binary plots of laser-ablation inductively coupled plasma mass spectrometry (LA-ICP-MS) data for pairs of trace elements with high to low levels of covariance throughout Pyrite 2 from sample 08-SP-155 from the Abbott-Wagner fracture-controlled replacement deposit. The variation of colours from blue to pink corresponds to an increase in point density: **i)** Cu vs. In; **j)** Ag vs. Sb; **k)** Cu vs. Ga; **l)** Ag vs. Ga; **m)** Cu vs. Sb; **n)** Sb vs. Pb; **o)** Cu vs. Au; and **p)** As vs. Au.

distributed as nano- and micro-inclusions of Cu sulfide minerals. Cadmium and zinc typically covary well because they are mainly hosted in sphalerite inclusions and fracture fills. Our petrographic observations are consistent with this: inclusions of chalcopyrite and sphalerite are present in the pyrite grains. The covariance between Ni and Co is good, especially in the rims of the pyrite grains (*see* Fig. 4).

Despite poor overall correlation between Au and As in FCR Py 2 (Fig. 12p), the positions of Au- and As-rich bands on element maps (Fig. 4) appear to correspond with each other. In order to robustly examine this apparent spatial correlation between As and Au, as well as other elements, we verified element covariations within specific isolated zones of the LA-ICP-MS maps using ioGAS (Fig. 13). Within the Au-rich zone (pink in Fig. 13), Au has a poor covariance with all elements, including As (R^2 = 0.25; Fig. 14), and within the As-rich zone (purple in Fig. 13), the Au-As correlation is only slightly better (R^2 = 0.41; Fig. 14). The best correlation between Au and As is in the Cu-rich core of the pyrite grain (grey in Fig. 13; R^2 = 0.60; Fig. 14), but the correlation is poor elsewhere. This implies that Au may not be hosted within the pyrite crystal lattice but may be present as micro-inclusions or nanoparticles of native Au or another Au-bearing phase.

In the Cu-rich zones (grey and brown in Fig. 13), Cu has good covariance with Ag, Ga, Ge, and Sn (R^2 = 0.53–0.79; Fig. 15); however, the Cu-Au and Cu-As correlations overall are poor in the zones mentioned above (and in the whole pyrite grains; Fig. 12o), except for two subsets of high Au values in the Au- and As-rich zones (R^2 = 0.53 and 0.84, respectively; Fig. 16).

Pyrite 3

The trace-element content of Py 3 from MVT deposits can be variable. In the Duncan deposit (sample 08-SP-121), the Py 3 overgrowth on Py 1 has higher Ni, Co, and As than adjacent Py 1 (Fig. 8) and Ni correlates well with Co (R^2 = 0.62).

In the Jersey-Emerald deposit (sample JS-07-56.9; Table 2), Py 3 has more Ni (140–1400 ppm, median 550 ppm), Co (11–68 ppm, median 23 ppm), Zn (97–140 000 ppm, median 26 000 ppm), Cd (4.6–1100 ppm, median 160 ppm), and Ag (0.1–66 ppm, median 10 ppm) than the other MVT Py 3 samples. In this sample, there is excellent correlation between Ni and Co (R^2 = 0.85), but not between the other elements determined.

Pyrite 3 from the Duncan deposit (sample 08-SP-121) has higher As (6.5–130 ppm, median 65 ppm) and Tl (0.07–92 ppm, median 0.07 ppm, with many outliers from 1 to 92 ppm) content than the other MVT Py 3 samples.

In Py 3 from the Jackpot Lerwick zone (sample 08-SP-102B), only Ga and Ge are more enriched than in the other MVT Py 3 samples. Here, Ga ranges from 0.03 to 43 ppm (median 0.03 ppm, standard deviation 1.4 ppm) and Ge ranges from 0.41 to 94 ppm (median 0.41 ppm, standard deviation 3.9 ppm).

Pyrite 3 from the FCR deposit is substantially more enriched in As and Au than Py 3 from MVT deposits, and contains Ni-Co–rich bands (R^2 = 0.75) on the rim of the grain (Fig. 4) that contain less of other determined elements.

DISCUSSION

Numerous studies on the trace-element content of pyrite have identified elements such as Cu, Pb, Zn, Ag, Au, Mo, Co, Ni, As, Sb, and Se as useful for providing information on the genesis of mineral deposits (Reich et al., 2005, 2013; Large et al., 2009, 2011; Deditius et al., 2014; Genna and Gaboury, 2015; Gadd et al., 2016). According to Large et al. (2009, 2011) and Gregory et al. (2015), sedimentary pyrite in marine carbonaceous black shales and mudstones associated with Zn-Pb and Au deposits are typically enriched in As, Ni, Pb, Cu, and Co, with median concentrations ranging from the hundreds to thousands of parts per million. These values are much higher than for Mo, Sb, Zn, and Se, which have median contents ranging from the tens to hundreds of parts per million, and for Ag, Cd, and Au, which have median concentrations ranging from tenths to tens of parts per million.

Pyrite 1 in the Kootenay Arc MVT deposits has higher Ag, Ba, Cu, Ge, Pb, Sb, Sr, Tl, and V than adjacent Py 3 (Fig. 8; Table 2), and higher Ag, Au, Ba, Cu, Ge, Pb, and Tl than Py 2. These elements range in abundance from tenths to hundreds of parts per million, except Pb, which ranges from hundreds to hundreds of thousands of parts per million (high Pb values are due to galena micro-inclusions). The enrichment in V, Ba, and Sr is likely due to the presence of carbonate (or other nonsulfide mineral) inclusions in Py 1. This is supported by the positive correlation between Sr and CaO (R^2 = 0.78), MgO (R^2 = 0.51), and MnO (R^2 = 0.56) in Py 1. The enrichment in Cu, Ag, and Pb is likely due to the presence of sulfide mineral micro-inclusions. There are decreasing Tl median values from the early (Py 1) to later (Py 2 and Py 3) pyrite stages (Table 2), which correlates with a concomitant increase in Sb and Ni. Such a correlation may be explained by a coupled substitution between these elements into the pyrite structure (e.g. $2Fe^{2+} \leftrightarrow Tl + Sb^{3+}$; George et al., 2019). Given that Tl-bearing minerals have not been observed in any pyrite or deposits of the Kootenay Arc, the element is likely present as lattice substitutions in pyrite; however, the presence of

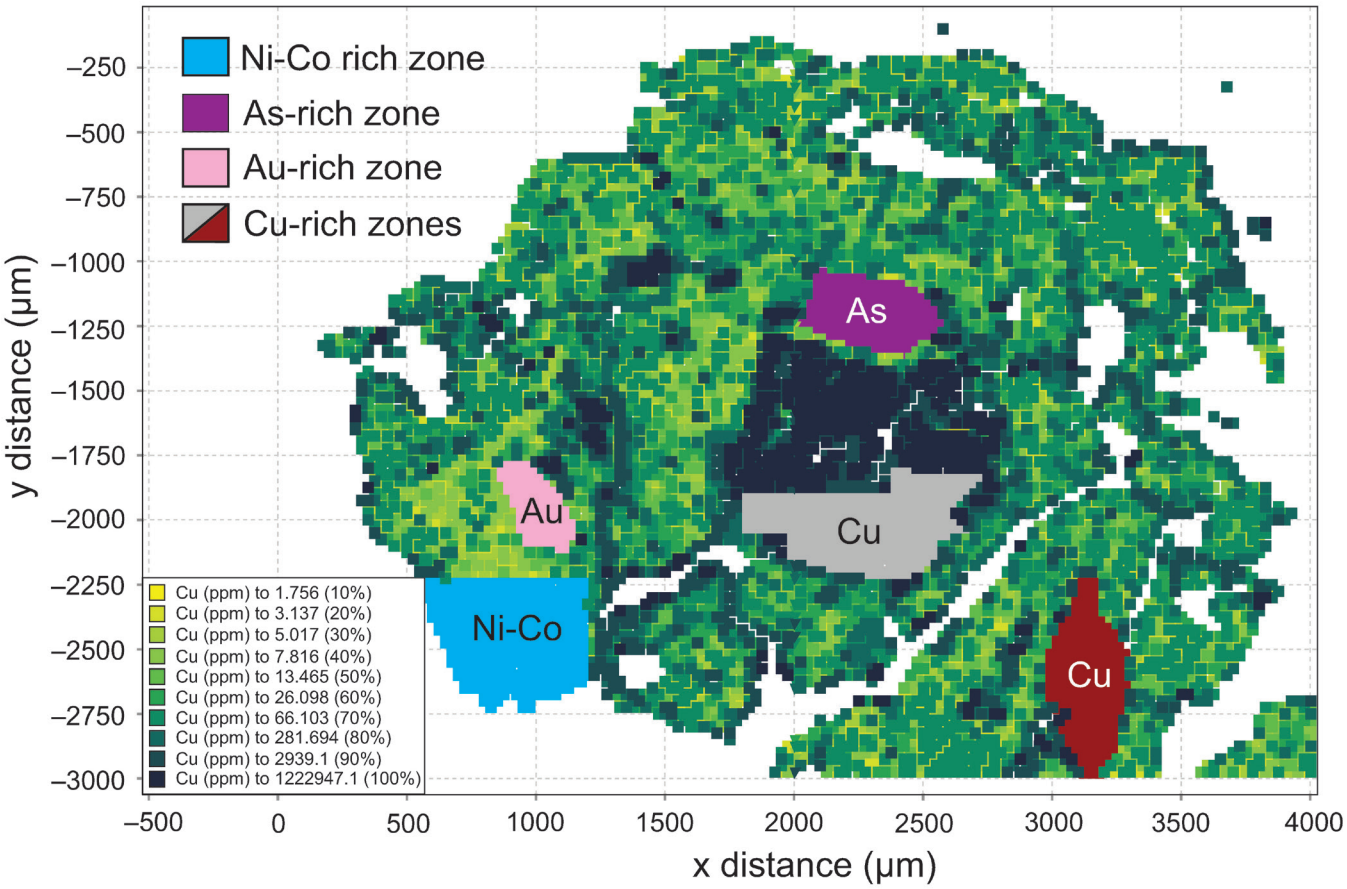

Figure 13. A laser-ablation inductively coupled plasma mass spectrometry (LA-ICP-MS) Cu distribution map of a pyrite grain, sample 08-SP-155 from the Abbott-Wagner fracture-controlled replacement deposit, generated using ioGAS software, showing selected zones enriched in specific elements.

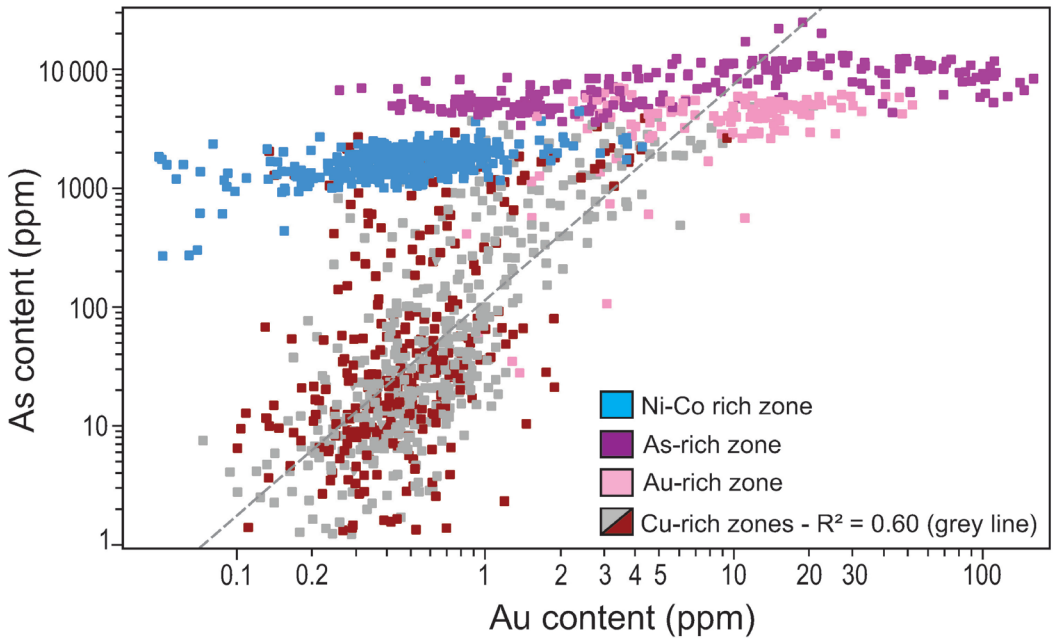

Figure 14. Binary plot of As vs. Au in Py 2 of sample 08-SP-155 from the Abbott-Wagner fracture-controlled replacement deposit in the selected enriched zones shown in Figure 13; the correlation coefficient (R^2) between As and Au in the Au-rich zone and As-rich zone is 0.25 and 0.41, respectively.

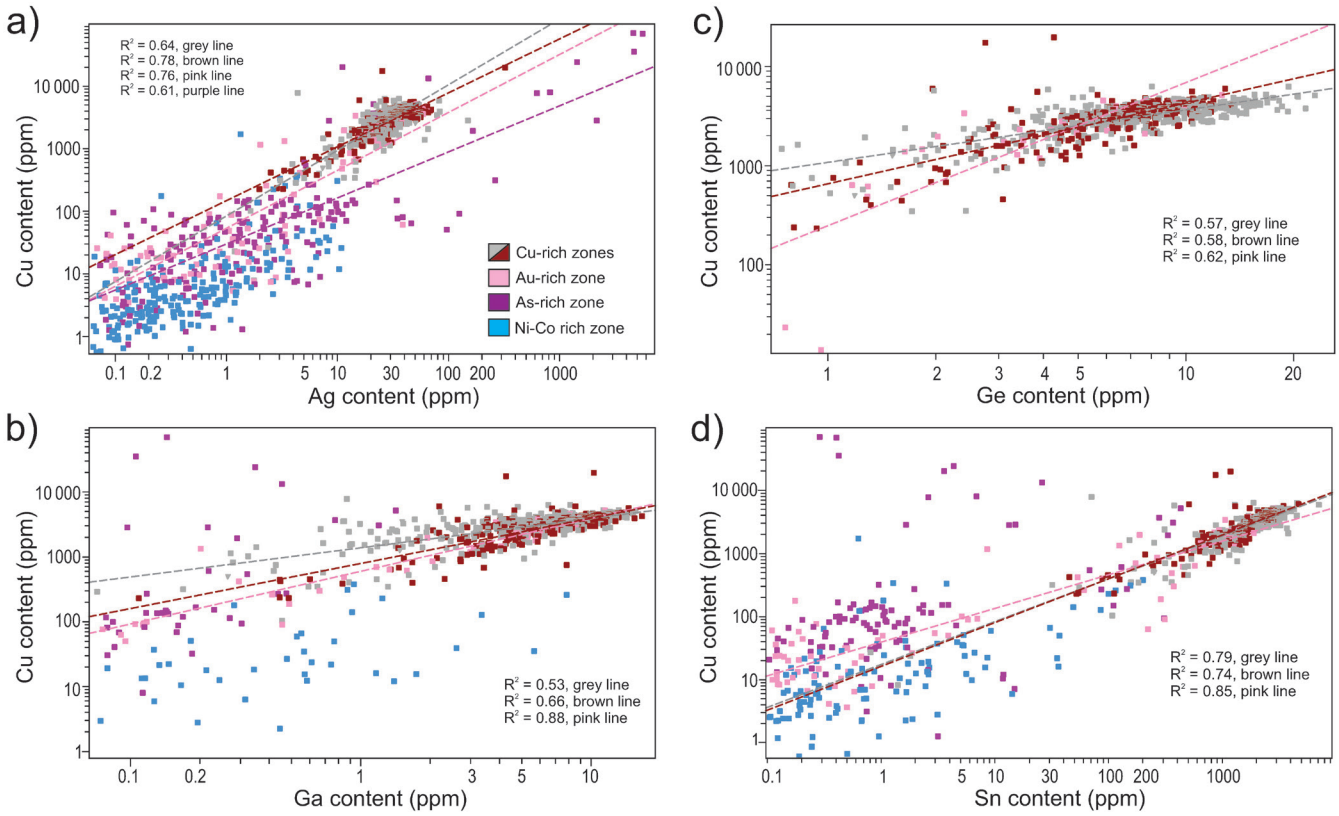

Figure 15. Binary plots of Cu vs. selected trace elements in Py 2 of sample 08-SP-155 from the Abbott-Wagner fracture-controlled replacement deposit in the selected enriched zones shown in Figure 13. The best covariance between Cu and **a)** Ag; **b)** Ga; **c)** Ge; and **d)** Sn occurs in the Cu-rich and Au-rich zones.

homogeneously distributed nanoparticles cannot be dismissed. Early sedimentary pyrite typically has high Tl values compared to later pyrite, especially pyrite of metamorphic origin (George et al., 2019). Arsenic, nickel, cobalt, and copper values in Py 1 range from tenths to hundreds of parts per million. Nickel in Py 1 ranges from 2.8 to 120 ppm with a median of 24 ppm, and Co ranges from the lower limit of detection (i.e. 0.21 ppm) to 2.8 ppm. The Co-Ni ratios in Py 1 range from 0.002 to 0.1 (Table 3) and plot within the sedimentary (low temperature) field of Figure 17 (*see* the Co-Ni ratios in pyrite section), slightly lower than that of sedimentary pyrite in marine black shales and mudstones, which typically have values from 0.01 to 2 (Large et al., 2009, 2011; Gregory et al., 2015). The Co-Ni ratios in Py 1 support our interpretation of Py 1 having a sedimentary origin; however, a hydrothermal origin could also explain some of the trace-element signatures and assemblages observed with these pyrite grains (such as low Co, Ni, As, Se, Mo, Sb, and Au values). Alternatively, the carbonate host rocks of the Duncan deposit, in which Py 1 was analyzed, may be depleted in these trace elements.

The hydrothermal pyrite (Py 2) samples from the MVT deposits have lower trace-element contents than Py 2 from the FCR deposit, except for Co, Ni, Mo, Ba, Tl, and Pb (Fig. 10). Overall, the trace-element contents in all pyrites from MVT deposits are low and in the range of tenths to thousands of parts per million, with the exception of Zn and Pb, which reach hundreds of thousands of parts per million (Table 2), likely due to sphalerite and galena inclusions in pyrite. The Au content of pyrite in MVT deposits is low (close to the lower limit of detection), with average Au typically less than 0.15 ppm.

Overall, the low trace-element content in pyrite from Kootenay Arc MVT deposits may be due to recrystallization and remobilization of impurities during post-mineralization metamorphism. Significant modification of primary trace-element distribution due to hydrothermal reworking, recrystallization, and metamorphism has been documented in many sediment-hosted deposits (Large et al., 2011; Gregory et al., 2015); however, given that some primary pyrite textures are preserved and growth-related element zonation is absent in MVT Py 1 and Py 2, and that they retain their primary trace-element signatures, it is likely that the trace-element signature is characteristic of pyrite from MVT deposits in the Kootenay Arc and that subsequent events have not significanly erased their primary trace-element signatures.

In Py 2 from the Abbott-Wagner FCR deposit, Cu, Zn, Ga, As, Ag, In, Sn, Sb, and Au are among the most abundant trace elements, and enrichment of these elements follows growth bands (Fig. 11). Such growth bands can be

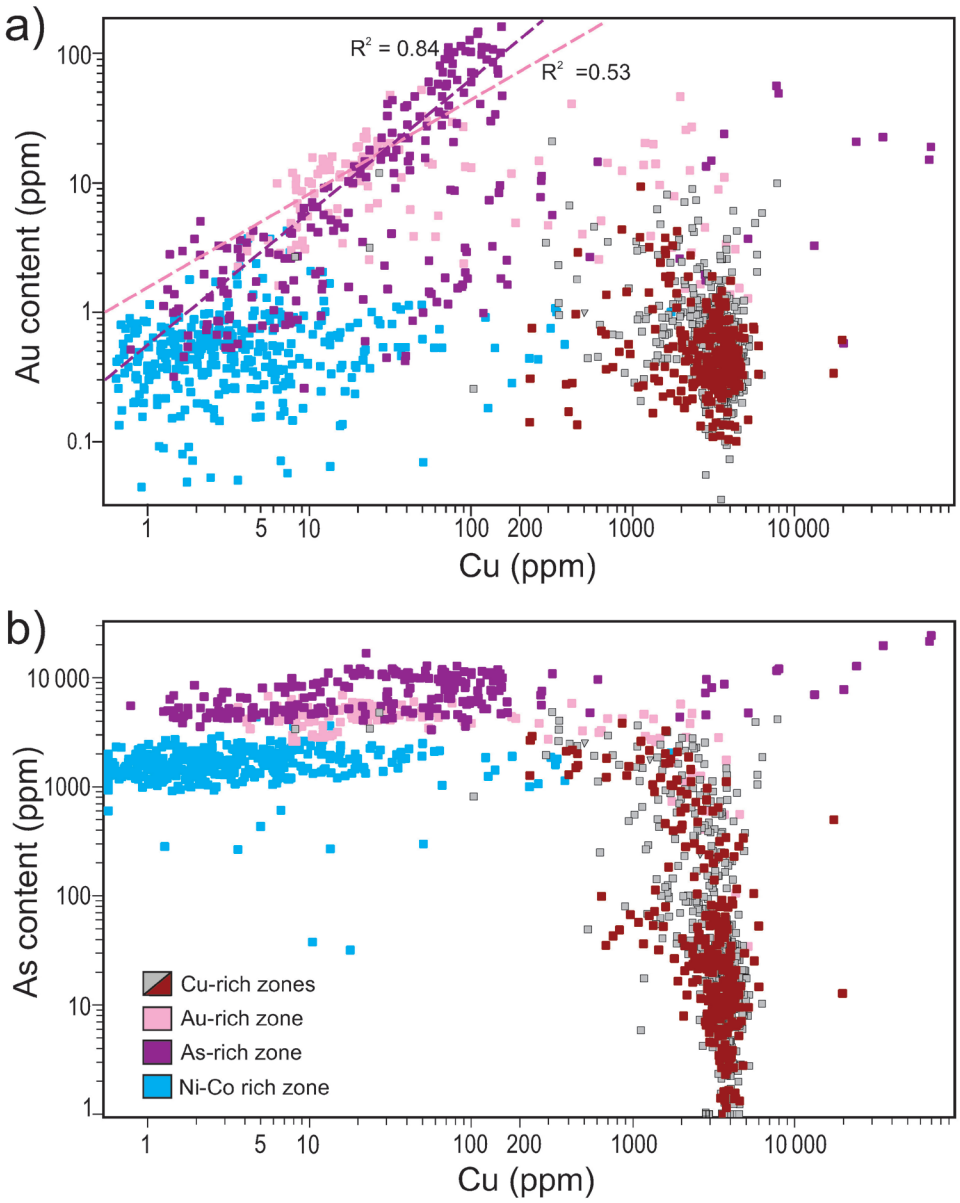

Figure 16. Binary plots in Py 2 of sample 08-SP-155 from the Abbott-Wagner fracture-controlled replacement deposit in the selected enriched zones shown in Figure 13: **a)** Au vs. Cu results in correlation coefficients (R^2 = 0.53 and R^2 = 0.84) corresponding to high Au values in the Au- and As-rich zones, respectively. Overall the correlation between Au and Cu for the different zones is poor; **b)** As vs. Cu displays tight vertical and horizontal arrays, suggesting that these two elements are independent and uncorrelated.

attributed to lattice-bound elements or syntaxial crystallization of related phases, rather than nanoparticles or micro-inclusions. This strong zonation may indicate a series of pyrite growth events or evolution of the fluid trace-element content during pyrite crystallization (George et al., 2018; Nadoll et al., 2019). The LA-ICP-MS trace-element analyses of sphalerite in this deposit show similar element zonation along growth bands, suggesting compositional changes of the mineralizing fluid with time (S. Paradis, unpub. data, 2019). Although the Abbott-Wagner FCR deposit was affected by lower greenschist facies regional metamorphism, the primary trace-element signatures in pyrite are unaffected. Enrichment in Au (and other elements) does not appear to be related to deformation-induced microstructures, suggesting that prograde metasomatism associated with regional deformation is likely not the source of Au-bearing hydrothermal fluids in this deposit. Pyrite 2 in this FCR deposit is especially rich in Au (tenths to hundreds of parts per million) and As (tens to tens of thousands of parts per million), but microscopic examination of the sample analyzed from this deposit did not reveal any particles of Au phases (electrum, native Au) in pyrite and other sulfide

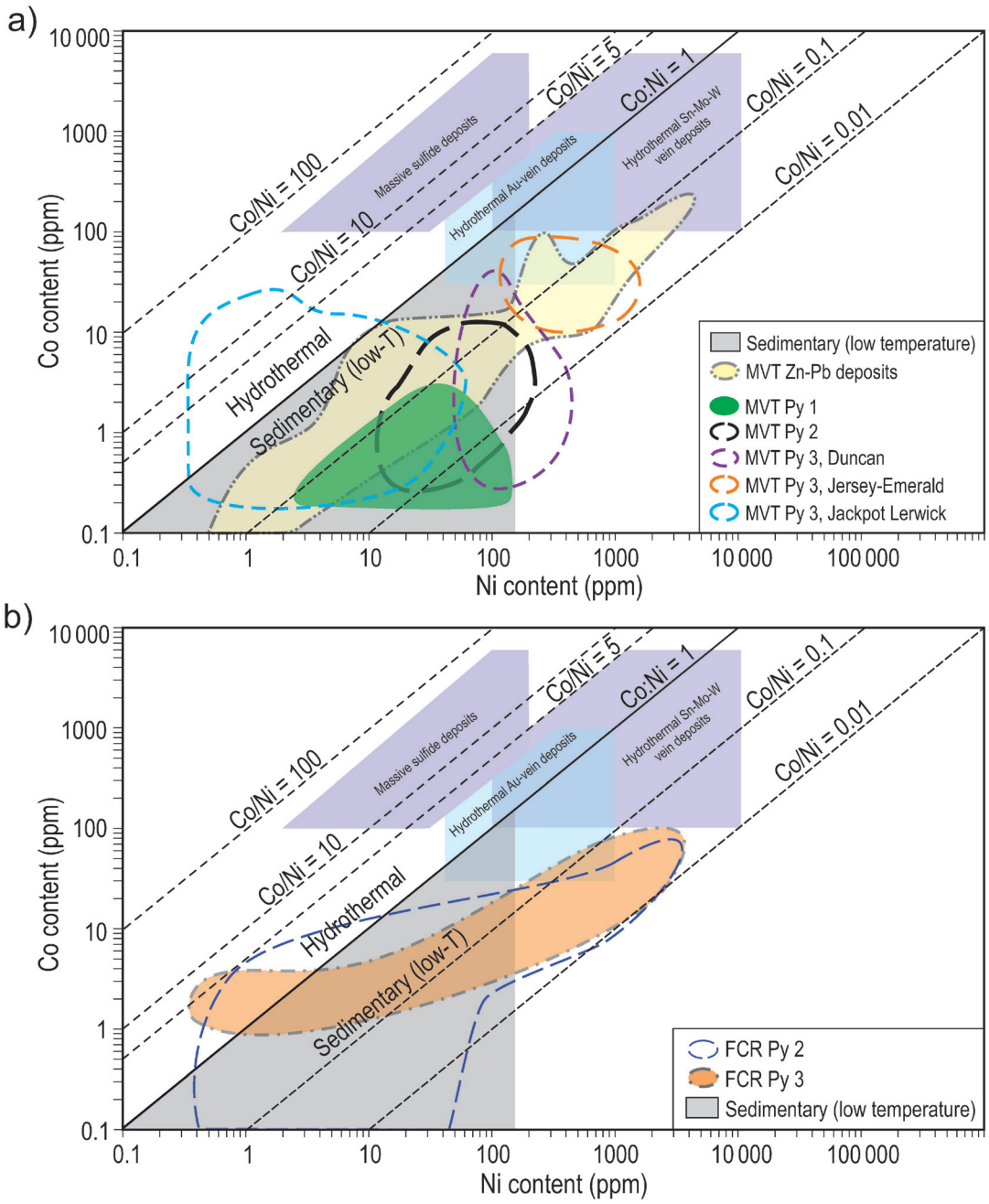

Figure 17. Discriminant diagrams of Co vs. Ni for pyrite *modified from* Price (1972), Campbell and Ethier (1984), and Nadoll et al. (2019). The sedimentary (low temperature) field is typical of pyrite with Co-Ni ratios less than 1; whereas hydrothermal pyrite has highly variable Co-Ni ratios (>1, commonly >10): **a)** pyrite 1, 2, and 3 from the Reeves MacDonald, Jersey-Emerald, Jackpot Lerwick, and Duncan Mississippi Valley–type (MVT) deposits. The MVT Zn-Pb field is *after* Meng et al. (2019) and includes data from the Jinding and Hoshbulak MVT Zn-Pb deposits, China (Li et al., 2015; Wang et al., 2018); **b)** Pyrite 2 and 3 from the Abbott-Wagner fracture-controlled replacement (FCR) deposit. With the exception of some of the high Co/low Ni MVT Py 3 grains from Jackpot Lerwick, and some of the high Co/low Ni FCR Py 2 and Py 3 grains from Abbott-Wagner, all of the pyrite grains from the Kootenay Arc deposits fall in the sedimentary and MVT Zn-Pb fields.

minerals. The LA-ICP-MS maps of FCR Py 2 revealed growth bands rich in Au and As; however, these bands of Au- and As-enrichment are not coincident and there is poor correlation between Au and As for discrete growth bands, and in the pyrite grains as a whole. This indicates that Au may be controlled (at least in part) by Au-bearing nanoparticles or micro-inclusions in pyrite and may not be entirely lattice hosted. Gold in this Py 2 is also poorly correlated with all the other elements, including Ag, Cu, Pb, and Sb.

Pyrite 2 in the FCR sample has elevated Cu, Zn, Ga, As, Ag, In, Sn, Sb, and Au (tenths to hundreds of thousands of parts per million; Table 2). These trace elements are characteristic of the polymetallic nature of the Abbott-Wagner FCR deposit and of the mineral association represented by galena, sphalerite, and pyrite with traces of chalcopyrite and tetrahedrite. Although pyrite can incorporate a wide array of trace metals, such as Ag, As, Au, Bi, Co, Cu, Hg, Mo, Ni, Pb, Pd, Ru, Sb, Se, Te, Tl, and Zn, as stoichiometric and non-stoichiometric substitutions in the crystal lattice (Huston et al., 1995; Abraitis et al., 2004; Reich et al., 2005; Large et al., 2009; Deditius et al., 2014; Cook et al., 2016), such high values of Ag, Cu, Zn, Sn, and Sb in FCR Py 2 are likely due to the presence of nanoparticles or micro-inclusions in the pyrite. Micro-inclusions of carbonate, sphalerite, and chalcopyrite were observed in FCR Py 2 during petrographic microscope analysis.

Pyrite 3 in both MVT and FCR deposits has low concentrations of most elements, except for Ni, Co, As (±Au). The depletion in most elements is similar to the depletion documented in the latest stage of pyrite growth (i.e. associated with deformation, metamorphism, and recrystallization) in carbonaceous black shales and mudstones, which can be associated with Zn-Pb and Au deposits (Large et al., 2007, 2009; Gregory et al., 2015; Gadd et al., 2016; Leighton et al., 2019); however, the enrichment of Ni, Co, and As in Py 3 is contrary to observations made by the above authors on late pyrite. Loss or gain of elements can be due to post-depositional recrystallization during hydrothermal and metamorphic processes (Large et al., 2007, 2009, 2011); however, Ni and Co are not readily released during hydrothermal and metamorphic pyrite recrystallization (Large et al., 2009; Koglin et al., 2010).

In the Abbott-Wagner FCR deposit, Py 3 is more enriched in Au and As than it is in MVT deposits (Table 2). This is consistent with the high Au and As content found in Py 2 and other sulfide minerals (e.g. sphalerite) of the Abbott-Wagner FCR deposit. Pyrite 3 from the FCR deposit forms Ni- and Co-rich bands (R^2 = 0.75) on the rim of the pyrite grain (Fig. 4), and these bands have lower concentrations of other elements. The Ni- and Co-rich bands on the rim of the analyzed pyrite grain are attributed to euhedral metamorphic overgrowths (e.g. Large et al., 2007; Gadd et al., 2016).

Co-Ni ratios in pyrite

Chemical signatures of pyrite (and other sulfide minerals) can aid in deciphering the complex evolution of mineral deposits and can be used to 'fingerprint' different types of mineralization (Huston et al., 1995; Large et al., 2009, 2011; Gourcerol et al., 2018; Meng et al., 2019).The Co-Ni ratio in pyrite is widely used to characterize the depositional setting and origin of pyrite formation (e.g. discriminating between sedimentary and hydrothermal; Loftus-Hills and Solomon, 1967; Price, 1972; Bralia et al., 1979; Gregory et al., 2015; Nadoll et al., 2019). A low Co-Ni ratio (i.e. <1) typically represents sedimentary pyrite or pyrite associated with sediment-hosted deposits. Higher and highly variable Co-Ni ratios (>1 and commonly >10) are thought to be the result of hydrothermal processes; however, Price (1972) showed that numerous hydrothermal pyrites have Co-Ni ratios of less than 1.0, and that low Co-Ni ratios are not necessarily indicative of sedimentary pyrite. The Co-Ni ratio should not be used in isolation and should be used in conjunction with other criteria — the most important being geological and petrographic information (Bralia et al., 1979; Bajwah et al., 1987).

The Co-Ni discrimination diagrams (Fig. 17) illustrate that most of the pyrites analyzed (Py 1, Py 2, and Py 3) from the Kootenay Arc deposits have Co-Ni ratios below 1 and plot within the sedimentary field. A cluster of data points with high Co-Ni ratios (1–35) corresponds to As-rich zones in Py 3 from the MVT Jackpot Lerwick zone. This Py 3 is fractured and surrounded by deformed aggregates of pyrrhotite and sphalerite that are oriented parallel to regional foliation. Another cluster of data points from FCR Py 2 and Py 3 (Abbott-Wagner deposit) have Co-Ni ratios between 1 and 5, but the majority of the data from this deposit plot within the low-temperature sedimentary and MVT fields, as defined by Price (1972) and Meng et al. (2019), respectively. The low Co-Ni ratios of these pyrites, especially FCR Py 2, are intriguing because we interpret them to be of hydrothermal origin so they should have higher Co-Ni ratios and not the low Co-Ni ratios that are more typical of a sedimentary origin. We believe that the Co and Ni content in the FCR and MVT pyrites from the Kootenay Arc deposits are the result of the low Ni and Co contents of the carbonate host rocks, which are below 20 ppm (S. Paradis, unpub. data, 2010), and not necessarily indicative of their environmental conditions during crystallization.

Our data show that, irrespective of their type (i.e. Py 1, Py 2, or Py 3), the majority of pyrite from MVT and FCR deposits plot in the low-temperature sedimentary field of Figure 17. The Co-Ni ratios of these pyrites reflect the low Ni and Co content of the sedimentary environment in which they formed; consequently, the ore-forming fluid that circulated in these carbonate rocks would have had low Co-Ni ratios. Additionally, the content of Co and Ni in pyrite from these deposits was most likely controlled by the low temperatures of ore-forming fluids in sedimentary environments.

Future work and outstanding questions

Work is ongoing to interpret LA-ICP-MS analyses of sphalerite from the carbonate-hosted deposits of the Kootenay Arc, and sulfide minerals from nearby Rocky Mountain MVT deposits. Simandl et al. (this volume) present LA-ICP-MS analyses of carbonate minerals associated with mineralization in the same deposits. The results of these two studies will be combined to provide insight into dolomite- and ore-forming fluid chemistry and origin in subsequent peer-reviewed publications.

CONCLUSIONS

Mississippi Valley–type (MVT) and fracture-controlled replacement (FCR) deposits in the Kootenay Arc share the same tectonostratigraphic setting and location along the distal western margin of Ancestral North America. In this study, we analyzed the spatial trace-element distribution in pyrite from these deposit types using an emerging technique and showed that they have distinct mineralogical, textural, and chemical characteristics. We highlighted the potential of pyrite trace-element geochemistry to indicate different mineralization types, which can have far-reaching implications for exploration strategies in the Kootenay Arc and in similar geological environments with carbonate-hosted Zn-Pb deposits. For example, pyrite with high content of Ag, Cu, Ga, In, Sb, Sn, Zn, and especially Au and As can indicate the presence of a polymetallic deposit rich in these elements (i.e. a carbonate-hosted polymetallic FCR deposit as opposed to a MVT Zn-Pb deposit).

Pyrite 1, which is interpreted as sedimentary or diagenetic, has only been observed in MVT deposits, whereas hydrothermal and metamorphic pyrite (Py 2 and Py 3, respectively) have been identified in both MVT and FCR deposits. Although element zonation is present in MVT pyrite (e.g. Py 1), rhythmic growth banding of elements has only been observed in FCR Py 2. Pyrite 1 is subhedral, inclusion-rich, overgrown by later pyrite generations, and is the earliest pyrite. Compared to adjacent Py 3, it has higher Na_2O, K_2O, CaO, MnO, MgO, Ag, Ba, Cu, Ge, Pb, Sb, Sr, Tl, and V. Compared to MVT Py 2, Py 1 has higher Ag, Au, Ba, Cu, Ge, Pb, and Tl. Pyrite 2 in MVT and FCR deposits is moderately rich in inclusions and occurs as individual, or clusters of anhedral to subhedral, fractured grains that can be overgrown by sphalerite, pyrrhotite, and Py 3. Relative to the Abbott-Wagner FCR deposit, Py 2 in MVT deposits is enriched in Ba, Co, Mo, Ni, Pb, and Tl and is depleted in other elements. In the Abbott-Wagner FCR deposit, Py 2 has cores enriched in Ag, Cu, Ga, Ge, In, Sn, and Zn, intermediate Au- and As-rich bands, and Co- and Ni-rich rims. Pyrite 3 in MVT and FCR deposits typically forms euhedral crystals that display 120° triple junctions. It can form overgrowths on pre-existing pyrite and it is interpreted to result from the metamorphic recrystallization of earlier pyrite. Pyrite 3 is enriched in Co and Ni, particularly near overgrowths or infillings by sphalerite. The contrasting geochemical signatures of these MVT and FCR pyrites reflect the specific mineral compositions associated with the two deposit types that is the low and high contents of specific trace elements in MVT and FCR deposits, respectively. The high contents of Ag, As, Au, Cu, Ga, In, Sb, Sn, and Zn in FCR Py 2 is characteristic of the polymetallic nature and mineral association (i.e. galena, sphalerite, pyrite, chalcopyrite, and tetrahedrite) of FCR deposits. This can be used as a pathfinder to explore for such deposit types in the Kootenay Arc.

ACKNOWLEDGMENTS

This study is a contribution to NRCan's Targeted Geoscience Initiative program (TGI-5). Support for this study was provided through the Volcanic- and Sedimentary-hosted Base Metal Mineralization project's Activity VS-2.1: Is there a genetic link between various types of sediment-hosted deposits of the Canadian Cordillera? and the Specialty Metals Ore Systems project. We thank Dr. Randy Enkin for his insightful discussion and introduction to ioGAS techniques. The paper benefited from the comments and suggestions of Jean-Luc Pilote (Geological Survey of Canada) and an anonymous reviewer. The clarity of the manuscript was also improved by Connor Robinson (British Columbia Geological Survey). We thank Jan Peter (Geological Survey of Canada) for editorial handling.

REFERENCES

Abraitis, P.K., Pattrick, R.A.D., and Vaughan, D.J., 2004. Variations in the compositional, textural and electrical properties of natural pyrite: a review; International Journal of Mineral Processing, v. 74, no. 1-4, p. 41–59. https://doi.org/10.1016/j.minpro.2003.09.002

Apex Mineral Resources Inc., Jersey Emerald property; Apex Mineral Resources Inc. <http://www.sultanminerals.com/s/Jersey_Emerald.asp> [accessed March 26, 2020]

Bajwah, Z.U., Seccombe, P.K., and Offler, R., 1987. Trace element distribution, Co:Ni ratios and genesis of the Big Cadia iron-copper deposit, New South Wales, Australia; Mineralium Deposita, v. 22, p. 292–300. https://doi.org/10.1007/BF00204522

Bradley, O.E., 1970. Geology of the Jersey lead-zinc mine, Salmo, British Columbia; Chapter 8 *in* Lead-zinc deposits of the Kootenay Arc, northeastern Washington and adjacent British Columbia, (ed.) A.E. Weissenborn, F.C. Armstrong, and J.T. Fyles; Washington State Department of Natural Resources, Division of Mines and Geology, Bulletin 61, p. 89–98.

Bralia, A., Sabatini, G., and Troja, F., 1979. A revaluation of the Co/Ni ratio in pyrite as geochemical tool in ore genesis problems; Mineralium Deposita, v. 14, no. 3, p. 353–374. https://doi.org/10.1007/BF00206365

British Columbia Geological Survey, 1991. MINFILE 082FSW012 record summary, MINFILE BC mineral deposits database; British Columbia Ministry of Energy, Mines and Petroleum Resources, British Columbia Geological Survey. <https://minfile.gov.bc.ca/Summary.aspx?minfilno=082FSW012> [accessed September 17, 2019]

British Columbia Geological Survey, 2011. MINFILE 082KNW056 record summary, MINFILE BC mineral deposits database; British Columbia Ministry of Energy, Mines and Petroleum Resources, British Columbia Geological Survey. <https://minfile.gov.bc.ca/Summary.aspx?minfilno=082KNW056> [accessed September 17, 2019]

Brown, R.L., Fyles, J.T., Glover, J.K., Höy, T., Okulitch, A.V., Preto, V.A., and Read, P.B., 1981. Southern Cordillera cross-section – Cranbrook to Kamloops; *in* Field guides to geology and mineral deposits; Geological Association of Canada, p. 335–371.

Campbell, F.A. and Ethier, V.G., 1984. Nickel and cobalt in pyrrhotite and pyrite from the Faro and Sullivan orebodies. Canadian Mineralogist, v. 22, p. 503–506.

Colpron, M. and Price, R.A., 1995. Tectonic significance of the Kootenay terrane, southeastern Canadian Cordillera: an alternative model; Geology, v. 23, no. 1, p. 25–28. https://doi.org/10.1130/0091-7613(1995)023%3C0025:TSOTKT%3E2.3.CO;2

Cook, N., Ciobanu, C.L., George, L., Zhu, Z-Y., Wade, B., and Ehrig, K., 2016. Trace element analysis of minerals in magmatic-hydrothermal ores by laser ablation inductively-coupled plasma mass spectrometry: approaches and opportunities; Minerals, v. 6, no. 4, p. 1–34. https://doi.org/10.3390/min6040111

Cui, Y., Miller, D., Nixon, G., and Nelson, J., 2015. British Columbia digital geology; British Columbia Ministry of Energy and Mines, British Columbia Geological Survey, Open File 2015-2, 1 .zip file.

Deditius, A.P., Reich, M., Kesler, S.E., Utsunomiya, S., Chryssoulis, S.L., Walshe, J., and Ewing, R.C., 2014. The coupled geochemistry of Au and As in pyrite from hydrothermal ore deposits; Geochimica et Cosmochimica Acta, v. 140, p. 644–670. https://doi.org/10.1016/j.gca.2014.05.045

Dehnavi, S.A., McFarlane, C.R.M., Lentz, D.R., and Walker, J.A., 2018. Assessment of pyrite composition by LA-ICP-MS techniques from massive sulphide deposits of the Bathurst mining camp, Canada: from textural and chemical evolution to its application as a vectoring tool for the exploration of VMS deposits; Ore Geology Reviews, v. 92, p. 656–671. https://doi.org/10.1016/j.oregeorev.2017.10.010

Fyles, J.T., 1964. Geology of the Duncan Lake area, Lardeau district, British Columbia; British Columbia Department of Mines and Petroleum Resources, Bulletin 49, 87 p.

Fyles, J.T. and Hewlett, C., 1959. Stratigraphy and structure of the Salmo lead-zinc area; British Columbia Department of Mines, Bulletin 41, 162 p.

Gabrielse, H., Monger, J.W.H., Wheeler, J., and Yorath, C.J., 1991. Part A – Morphogeological belts, tectonic assemblages and terranes; Chapter 2 *in* Geology of the Cordilleran Orogen in Canada, (ed.) H. Gabrielse and C.J. Yorath; Geological Survey of Canada, Geology of Canada Series, no. 4 (also Geological Society of America, The Geology of North America, v. G-2.), p. 15–28. https://doi.org/10.4095/134069

Gadd, M.G., Layton-Matthews, D., Peter, J.M., and Paradis, S., 2016. The world class Howard's Pass SEDEX Zn-Pb district, Selwyn Basin, Yukon. Part I: Trace element compositions of pyrite record input of hydrothermal, diagenetic and metamorphic fluids to mineralization; Mineralium Deposita, v. 51, no. 3, p. 319–342. https://doi.org/10.1007/s00126-015-0611-2

Genna, D. and Gaboury, D., 2015. Deciphering the hydrothermal evolution of a VMS system by LA-ICP-MS using trace elements in pyrite: an example from the Bracemac-McLeod deposits, Abitibi, Canada, and implications for exploration; Economic Geology, v. 110, p. 2087–2108. https://doi.org/10.2113/econgeo.110.8.2087

George, L.L., Biagioni, C., D'Orazioa, M. and Cook, N.J., 2018. Textural and trace element evolution of pyrite during greenschist facies metamorphic recrystallization in the southern Apuan Alps (Tuscany, Italy): influence on the formation of Tl-rich sulfosalt melt; Ore Geology Reviews, v. 102, p. 59–105. https://doi.org/10.1016/j.oregeorev.2018.08.032

George, L.L., Biagioni, C., Lepore, G.O., Lacalamita, M., Agrosì, G., Capitani, G.C., Bonaccorsi, E., and d'Acapito, F., 2019. The speciation of thallium in (Tl,Sb,As)-rich pyrite; Ore Geology Reviews, v. 107, p. 364–380. https://doi.org/10.1016/j.oregeorev.2019.02.031

Giroux, G. and Grunenberg, P., 2014. Technical report for the Jersey-Emerald property, Salmo, BC; Margaux Resources Ltd., 99 p.

Gourcerol, B., Kontak, D.J., Thurston, P.C., and Petrus, J.A., 2018. Results of LA-ICP-MS sulfide mapping from Algoma-type BIF gold systems with implications for the nature of mineralizing fluids, metal sources, and deposit models; Mineralium Deposita, v. 53, no. 6, p. 871–894. https://doi.org/10.1007/s00126-017-0788-7

Gregory, D.D., Large, R.R., Halpin, J.A., Baturina, E.L., Lyons, T.W., Wu, S., Danyushevsky, L., Sack, P.J., Chappaz, A., and Maslennikov, V.V., 2015. Trace element content of sedimentary pyrite in black shales; Economic Geology, v. 110, no. 6, p. 1389–1410. https://doi.org/10.2113/econgeo.110.6.1389

Guillong, M., Hametner, K., Reusser, E., Wilson, S.A., and Günther, D., 2005. Preliminary characterisation of new glass reference materials (GSA-1G, GSC-1G, GSD-1G and GSE-1G) by laser ablation-inductively coupled plasma-mass spectrometry using 193 nm, 213 nm and 266 nm wavelengths; Geostandards and Geoanalytical Research, v. 29, no. 3, p. 315–331. https://doi.org/10.1111/j.1751-908X.2005.tb00903.x

Halicz, L. and Günther, D., 2004. Quantitative analysis of silicates using LA-ICP-MS with liquid calibration; Journal of Analytical Atomic Spectrometry, v. 19, no. 12, p. 1539–1545. https://doi.org/10.1039/b410132d

Höy, T., 1982. Stratigraphic and structural setting of stratabound lead-zinc deposits in southeastern British Columbia; CIM Bulletin, v. 75, no. 840, p. 114–134.

Huston, D.L., Sie, S.H., Suter, G.F., Cooke, D.R., and Both, R.A., 1995. Trace elements in sulfide minerals from eastern Australian volcanic- hosted massive sulfide deposits: Part I. Proton microprobe analyses of pyrite, chalcopyrite, and sphalerite, and Part II. Selenium levels in pyrite: comparison with $\delta^{34}S$ values and implications for the source of sulfur in volcanogenic hydrothermal systems; Economic Geology, v. 90, p. 1167–1196. https://doi.org/10.2113/gsecongeo.90.5.1167

Jochum, K.P., Nohl, U., Herwig, K., Lammel, E., Stoll, B., and Hofmann, A.W., 2005. GeoReM: a new geochemical database for reference materials and isotopic standards; Geostandards and Geoanalytical Research, v. 29, no. 3, p. 333–338. https://doi.org/10.1111/j.1751-908X.2005.tb00904.x

Katay, F., 2017. Exploration and mining in the southeast region, British Columbia; *in* Exploration and Mining in British Columbia, 2016; British Columbia Ministry of Energy and Mines, British Columbia Geological Survey, Information Circular 2017-1, p. 73–107.

Koglin, N., Frimmel, H.E., Minter, W.L., and Brätz, H., 2010. Trace-element characteristics of different pyrite types in Mesoarchaean to Palaeoproterozoic placer deposits; Mineralium Deposita, v. 45, p. 259–280. https://doi.org/10.1007/s00126-009-0272-0

Large, R.R., Maslennikov, V.V., Robert, F., Danyushevsky, L.V., and Chang, Z.S., 2007. Multistage sedimentary and metamorphic origin of pyrite and gold in the giant Sukhoi Log deposit, Lena gold province, Russia; Economic Geology, v. 102, no. 7, p. 1233–1267. https://doi.org/10.2113/gsecongeo.102.7.1233

Large, R.R., Danyushevsky, L., Hollit, C., Maslennikov, V., Meffre, S., Gilbert, S., Bull, S., Scott, R., Emsbo, P., Thomas, H., Singh, B., and Foster, J., 2009. Gold and trace element zonation in pyrite using a laser imaging technique: implications for the timing of gold in orogenic and Carlin-style sediment-hosted deposits; Economic Geology, v. 104, no. 5, p. 635–668. https://doi.org/10.2113/gsecongeo.104.5.635

Large, R.R., Bull, S.W., and Maslennikov, V.V., 2011. A carbonaceous sedimentary source-rock model for Carlin-type and orogenic gold deposits; Economic Geology, v. 106, no. 3, p. 331–358. http://doi.org/10.2113/econgeo.106.3.331

Large, R.R., Halpin, J.A., Danyushevsky, L.V., Maslennikov, V.V., Bull, S., Long, J.A., Gregory, D.D., Lounejeva, E., Lyons, T., Sack, P.J., McGoldrick, P.J., and Calver, C.R., 2014. Trace element content of sedimentary pyrite as a new proxy for deep-time ocean-atmosphere evolution; Earth and Planetary Science Letters, v. 389, p. 209–220. https://doi.org/10.1016/j.epsl.2013.12.020

Lawley, C.J.M., Creaser, R., Jackson, S., Yang, Z., Davis, B., Pehrsson, S., Dubé, B., Mercier-Langevin, P., and Vaillancourt, D., 2015. Unravelling the Western Churchill Province Paleoproterozoic gold metallotectonic: constraints from Re-Os arsenopyrite and U-Pb xenotime geochronology and LA-ICP-MS arsenopyrite geochemistry at the BIF-hosted Meliadine gold district, Nunavut, Canada; Economic Geology, v. 110, no. 6, p. 1425–1454. https://doi.org/10.2113/econgeo.110.6.1425

Lawley, C.J.M., Jackson, S.E., Yang, Z., Davis, W., and Eglington, B.M., 2017. Tracing gold's transition from source to sponge to sink; Economy Geology, v. 112, no. 1, p. 169–183. https://doi.org/10.2113/econgeo.112.1.169

Leighton, C., Layton-Matthews, D., Peter, J.M., and Gadd, M.G., 2019. Application of pyrite chemistry to recognize a distal expression of hydrothermal activity in the MacMillan Pass SEDEX district, Yukon; *in* Targeted Geoscience Initiative: 2018 report of activities, (ed.) N. Rogers; Geological Survey of Canada, Open File 8549, p. 125–137. https://doi.org/10.4095/313646

Li, Z., Xue, C., Wu, Y., Dong, X., Wang, S., and Chen, J., 2015. The nappe-hosted Hoshbulak MVT Zn–Pb deposit, Xinjiang, China: a review of the geological, elemental and sTable isotopic constraints; Ore Geology Review, v. 70, p. 47–60. https://doi.org/10.1016/j.oregeorev.2015.03.019

Loftus-Hills, G. and Solomon, M., 1967. Cobalt, nickel and selenium in sulphides as indicators of ore genesis; Mineralium Deposita, v. 2, no. 3, p. 228–242. https://doi.org/10.1007/BF00201918

Meng, Y.M., Hu, R.Z., Huang, X.W., Gao, J.F., and Sasseville, C., 2019. The origin of the carbonate-hosted Huize Zn–Pb–Ag deposit, Yunnan province, SW China: constraints from the trace element and sulfur isotopic compositions of pyrite; Mineralogy and Petrology, v. 113, no. 3, p. 369–391. https://doi.org/10.1007/s00710-019-00654-2

Monger, J.W.H. and Price, R., 2002. The Canadian Cordillera: geology and tectonic evolution; Canadian Society of Exploration Geophysicists Recorder, v. 27, no. 2, p. 17–36.

Morse, J. and Luther, G., 1999. Chemical influences on trace metal-sulphide interactions in anoxic sediments; Geochimica et Cosmochimica Acta, v. 63, no. 19–20, p. 3373–3378. https://doi.org/10.1016/S0016-7037(99)00258-6

Moynihan, D.P. and Pattison, D.R.M., 2013. Barrovian metamorphism in the central Kootenay Arc, British Columbia: petrology and isograd geometry; Canadian Journal of Earth Sciences, v. 50, no. 7, p. 769–794. https://doi.org/10.1139/cjes-2012-0083

Muraro, T.W., 1962. Stratigraphy, structure and mineralization at Duncan mine, Lardeau district, British Columbia; M.Sc. thesis, Queen's University, Kingston, Ontario, 174 p.

Nadoll, P., Sośnicka, M., Kraemer, D., and Duschl, F., 2019. Post-Variscan structurally-controlled hydrothermal Zn-Fe-Pb sulfide and F-Ba mineralization in deep-seated Paleozoic units of the North German Basin: a review; Ore Geology Reviews, v. 106, p. 273–299. https://doi.org/10.1016/j.oregeorev.2019.01.022

Paradis, S., Bailey, S.L., Creaser, R.A., Piercey, S.J., and Schiarizza, P., 2006. Paleozoic magmatism and syngenetic massive sulphide deposits of the Eagle Bay assemblage, Kootenay terrane, southern British Columbia; *in* Paleozoic evolution and metallogeny of Pericratonic terranes at the ancient Pacific margin of North America, Canadian and Alaskan Cordillera, (ed.) M. Colpron and J.L. Nelson; Geological Association of Canada, Special Paper 45, p. 383–414.

Paradis, S., Keevil, H., Simandl, G.J., and Raudsepp, E., 2015. Carbonate-hosted nonsulphide Zn-Pb mineralization of southern British Columbia, Canada; Mineralium Deposita, v. 50, no. 8, p. 923–951.

Price, B.J., 1972. Minor elements in pyrites from the Smithers map area, B.C. and exploration applications of minor element studies; M.Sc. thesis, The University of British Columbia, 270 p.

Reich, M., Kesler, S.E., Utsunomiya, S., Palenik, C.S., Chryssoulis, S.L., and Ewing, R.C., 2005. Solubility of gold in arsenian pyrite; Geochimica et Cosmochimica Acta, v. 69, no. 11, p. 2781–2796. https://doi.org/10.1016/j.gca.2005.01.011

Reich, M., Deditius, A., Chryssoulis, S., Li, J.W., Ma, C.Q., Parada, M.A., Barra, F., and Mittermayr, F., 2013. Pyrite as a record of hydrothermal fluid evolution in a porphyry copper system: a SIMS/EMPA trace element study; Geochimica et Cosmochimica Acta, v. 104 (Suppl. C), p. 42–62. https://doi.org/10.1016/j.gca.2012.11.006

Sack, P.J., Large, R.R., and Gregory, D.D., 2018. Geochemistry of shale and sedimentary pyrite as a proxy for gold fertility in the Selwyn basin area, Yukon; Mineralium Deposita, v. 53, no. 7, p. 997–1018. https://doi.org/10.1007/s00126-018-0793-5

Tribovillard, N., Algeo, T.J., Lyons, T., and Riboulleau, A., 2006. Trace metals as paleoredox and paleoproductivity proxies: an update; Chemical Geology, v. 232, no. 1-2, p. 12–32. https://doi.org/10.1016/j.chemgeo.2006.02.012

Wang, C., Yang, L., Bagas, L., Evans, N.J, Chen, J., and Du, B., 2018. Mineralization processes at the giant Jinding Zn–Pb deposit, Lanping Basin, Sanjiang Tethys Orogen: Evidence from in situ trace element analysis of pyrite and marcasite; Geological Journal, v. 53, no. 4, p. 1279–1294. https://doi.org/10.1002/gj.2956

Warren, M.J. and Price, R.A., 1993. Tectonic significance of stratigraphic and structural contrasts between the Purcell Anticlinorium and the Kootenay Arc, east of Duncan Lake (82K); *in* Geological Fieldwork 1992, (ed.) B. Grant and J.M. Newell; British Columbia Ministry of Energy, Mines and Petroleum Resources, British Columbia Geological Survey, Paper 1993-01, p. 9–16.

Wheeler, J.O. and McFeely, P., 1991. Tectonic assemblage map of the Canadian Cordillera and adjacent parts of the United States of America; Geological Survey of Canada, Map 1712A, scale 1:2 000 000. https://doi.org/10.4095/133549